広島大学学位請求論文

Characterization of the automobile emission catalyst with nano structure using synchrotron radiation for high performance

放射光を用いたナノ構造を有する自動車用触媒の
高性能化に関する研究

2019 年

広島大学大学院理学研究科

物理科学専攻

國府田　由紀

目次

1. 主論文

Characterization of the automobile emission catalyst with nano structure using

synchrotron radiation for high performance

放射光を用いたナノ構造を有する自動車用触媒の高性能化に関する研究

2. 公表論文

● Fabrication and in/ex situ XPS Characterization of Rh Nanoparticles

Yuki Koda, Hirosuke Sumida, Satoshi Ogawa, Chie Tsukada and Hirofumi

Namatame

e-J. Surf. Sci. Nanotech. Vol. **15** (2017) 50-54

● Characterization by Synchrotron-Radiation X-Ray Photoelectron

Spectroscopy of NO Adsorption on Rh

Yuki Koda, Hirosuke Sumida, Satoshi Ogawa, Chie Tsukada and Hirofumi

Namatame

e-J. Surf. Sci. Nanotech. Vol. **16** (2018) 36-40

3. 参考論文

- Active three-way catalysis of rhodium particles with low oxidation state maintained under oxidation atmosphere on La-containing ZrO_2 support

Hisaya Kawabata, **Yuki Koda**, Hirosuke Sumida, Masahiko Shigetsu, Akihide Takami and Kei Inumaru

Chem. Commun., 2013, **49** (38), 4015 – 4017

- Self-regeneration of three-way catalyst rhodium supported on La-containing ZrO_2 in an oxidative atmosphere

Hisaya Kawabata, Yuki Koda, Hirosuke Sumida, Masahiko Shigetsu, Akihide Takami and Kei Inumaru

Catal. Sci. Technol., 2014, **4** (3), 697 – 707

- High three-way catalytic activity of rhodium particles on a Y-stabilized La-containing ZrO2 support: the effect of Y on the enhanced reducibility of rhodium and self-regeneration

Hisaya Kawabata, **Yuki Koda**, Hirosuke Sumida, Masahiko Shigetsu, Akihide Takami and Kei Inumaru

Catal. Sci. Technol., 2015, 5 (1), 584 – 594

4. 発表

- 放射光 XPS による NO 吸着前後の Rh ナノ粒子電子構造変化の解析

國府田　由紀、住田　弘祐、小川　智史、生天目　博文

第 53 回　X 線分析討論会（徳島大学）　　P18

- Characterization by Synchrotron-radiation X-ray photoelectron spectroscopy

  of NO adsorption on Rh nanoparticles.

Yuki Koda, Hirosuke Sumida, Satoshi Ogawa and Hirofumi Namatame

The 22nd Hiroshima International Symposium on Synchrotron Radiation

(Hiroshima University) P04.

- 放射光 XPS と理論計算による Rh ナノ粒子上での NO 吸着挙動

國府田　由紀、松本　祐樹、住田　弘祐、小川　智史、生天目　博文

第 54 回　X 線分析討論会（東京理科大学）　　P2-70

Doctoral Thesis

Characterization of the automobile emission catalyst with nano structure using synchrotron radiation for high performance

Yuki Koda

Graduate School of Science

Hiroshima University

January 2019

TABLE OF CONTENTS

Part Ⅰ

主論文

Chapter 1

General Introduction

Chapter 1: General Introduction

1.1   Environmental impacts of automobile emission

The emission from automobile has affected the urban air and human health with the industrial growing. The most significant emissions to the atmosphere are carbon dioxide (CO_2) and water vapor (H_2O) from the complete combustion of the fuel. However, depending on the combustion condition and the composition of the fuel, a small fraction of carbon monoxide (CO), unburned hydrocarbons (HC), nitrogen oxides (NO_X) and particulate matters are emitted. And, for example, sulfur dioxide (SO_2), NOx and some hydrocarbons cause 'acid rain', and CO_2, methane, N_2O and fluorocarbons cause 'Greenhouse effect' [1-4].

The first emission regulation was established in the 1970s in the United States, and was subsequently implemented in Europe and Japan. From the point of view of worldwide environmental protection, the emission regulation is getting stricter and stricter. To meet this present stringent regulation for automobile emission even after longtime driving for example 150 kmile in USA and to achieve the aim at 'Paris Agreement', catalyst technology plays a very important role in purifying exhaust gases [5].

Now, the automobile industry will undertake a big revolution in near future. Main cause is a request for reduction of CO_2 emissions. The aim at Paris Agreement adopted by COP21 in 2015 is to hold down the world average temperature rising to less than 2 degrees, same as before the Industrial Revolution. To realize this, the target in Japan is to reduce 26% of Green House Effect emission in 2013 by 2030, and more 90% by 2050. Therefore, development of the catalyst with higher conversion is emergent task [6].

1.2   Three-way catalysts

Three-way catalysts (TWC) have to promote the antagonizing reactions, oxidation of CO and HC and reduction of NOx giving the following reactions simultaneously [7].

$$C_yH_n + (1 + n/4)\ O_2\ \rightarrow\ yCO_2 + n/2\ H_2O$$

(1)

$$CO + 1/2\ O_2\ \rightarrow\ CO_2$$

(2)

$$CO + H_2O\ \rightarrow\ CO_2 + 1/2\ N_2 + CO_2 \tag{3}$$

$$NO\ (or\ NO_2) + CO\ \rightarrow\ 1/2\ N_2 + CO_2 \tag{4}$$

$$NO\ (or\ NO_2) + H_2\ \rightarrow\ 1/2\ N_2 + H_2O \tag{5}$$

$$(2 + n/2) \text{ NO (or NO}_2) + C_yH_n \rightarrow (1 + n/4) N_2 + yCO_2 + n/2 \ H_2O \qquad (6)$$
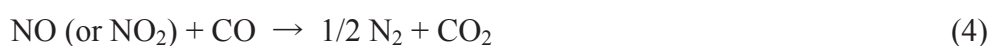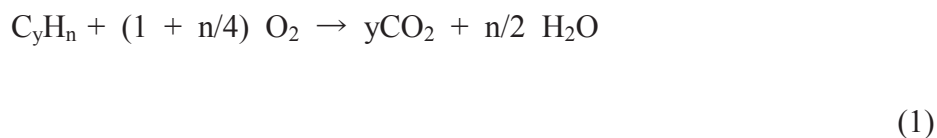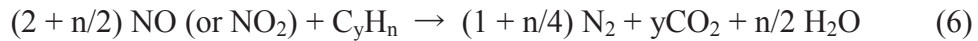
Fig.1-1 shows the typical example of the conversion of three main gases for air/fuel

ratio. The effective removal of three gases can be achieved at the stoichiometric ratio,

that is air by fuel (A/F) of 14.7. And it indicates that O_2 concentration in the exhaust

gas strongly affects the three-way catalytic activity.
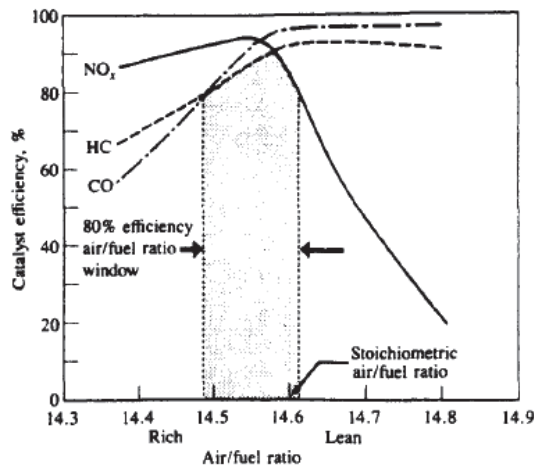
Fig.1-1. Conversion efficiency of NO, CO and HC as function of the air-fuel
ration in a three way catalytic converter [7].

The catalyst support is made of cordierite honeycomb or sometimes metallic

monolith coated with a thin activated washcoat which is made of Al_2O_3, OSC

component and some other additives loading some active components, for example

Platinum (Pt), Palladium (Pd) and rhodium (Rh) so on. For NO reduction, Rh is the

essential precious metal as the active site [7-9].

1.3 Demand for the three-way catalyst for HCCI engine

From the viewpoint of the prevention of global warming and the energy security, improvement in automobile fuel economy is strongly required and also improvement in thermal efficiency of internal combustion energies is urgently required. From many studies, increase of the expansion ratio or lean burn has shown effective for improving the thermal efficiency of gasoline engines in the Otto cycle [10, 11]. Therefore, there is a possibility that the form of engine combustion will shift from conventional SI combustion to lean burn in the future.

Demand for the three-way catalysis reaction has been changed with the engine development. As the exhaust emission becomes lower temperature and lean condition, performance of NO conversion is the key to meet the emission regulation. And catalysts need drastic changes to get over this object.

Rh shows excellent catalytic activity compared with the other precious metals (Pt, Pd, Ir and Ag), especially in NOx conversion [8,12,13]. Because Rh shows high activities towards NO dissociation which is the elementary step of NOx reduction, NOx is removed by reduction with CO or hydrocarbons [14]. However, the amount of Rh production is very small compared to other precious metals. The automotive industry uses almost 100% of the Rh production as exhaust catalysts. Therefore, in

view of resource saving, minimizing Rh amount is desirable. In other words, we need to enhance the catalytic activity of Rh using minimum amount of Rh.

And one way to make Rh more effective in NO reduction is minimizing the Rh particle size to maximize the number of reaction sites. As the metal particle size decreases below 10 nm, both different geometric and electronic properties can be observed in comparison with those of the bulk material. This is because surface activity is improved not only by increasing the surface area but also by introducing many surface structures having unsaturated bonds such as edges. And the bulk materials have a continuous electron level. On the other hand, nanoparticles have a discrete one and the band gap increases called "Kubo effect". By using this effect, the band gap of the semiconductor nanoparticles is controlled by the particle diameter, and the wavelength region in which the light emitting and receiving element can be changed. [15-19].

Another way to make Rh more effective in NO reduction is to control the electronic states relating to "adsorption and desorption behavior" of the reactant gases, which is the elementary step and plays significant role of catalytic reaction. For controlling the electronic state, nanoparticle/support interactions play a significant role affecting (i) the electronic structure of the nanoparticles through charge transfer processes, (ii)

the crystalline and electronic structure of the nanoparticles due to induced strain at the nanoparticle/support interface, or (iii) properties of interfacial sites (metal atoms at the perimeter of the nanoparticle in contact with the support) [16, 20-24].

1.4   Development of new catalyst for HCCI engine

The three-way catalyst for the next generation engine "HCCI" whose exhaust emission becomes lower temperature and lean condition must be developed, and this needs a drastic technical breakthrough. From now on, in order to improve the function of the material dramatically, it is not a conventional trial and error development, but Model Base Research (MBR), which is to clarify the mechanism of phenomenon and to develop a new material by modeling the ideal state, has become essential. The key to this is "analysis technology that can capture phenomena accurately" and "modeling calculation". In "Analytical technology", improving accuracy of analysis instruments, Synchrotron Radiation technology, in-situ analytical technologies and so on have enabled to understand the phenomenon more accurately. At the same time, in recent years, computer hardware and software in modeling calculation have leveled up to treat the part of the practical catalysts (a several precious metals and support material) [25-28].

As a first step for this study, it is necessary to understand "NO adsorption–

desorption behavior" which is the rate determining step of NO reduction and the relationship between its behavior with the electronic property of Rh used for active sites.

1.4.1   Characterization for understanding of catalytic performance

The first concern is the intrinsic properties of Rh nanoparticles(NPs). For this characterization of the electronic property, in-situ X-ray photoelectron spectroscopy (XPS) is adopted, *as* it is the suitable analytical method, excluding the influence of any adsorbed components. The second concern is the properties of Rh nanoparticles in a practical condition. A three-way catalyst operates under at ambient pressure under oxygen-rich condition as written in section 1.3. Oxygen atoms initially chemisorb on the metal surface and above a critical oxygen coverage, chemisorbed oxygen induces surface restructuring and the formation of surface oxides. Moreover, continued oxygen adsorption causes the surface oxide to transform to a multilayer bulk oxide. Because oxides and their parent metals usually have very different chemical properties, the transformation of a metal surface to a metal oxide shows the drastic change of catalytic performance [29-31]. For the above reason, the influence of oxygen for the electronic properties was

clarified.

Synchrotron radiation is an electromagnetic wave generated when electrons going straight at almost the speed of light are changed by a magnet or the like in the traveling direction. Synchrotron radiation has five main features. (i) High Brightness (ii) Including a wide wavelength range from X-rays to infrared rays (iii) Thinned narrowly, hard to spread (iv) Polarized (v) Repetition of a short pulse light. For analysis written above, synchrotron radiation is an effective method for (i) and (ii).

In this study, fabrication by the evaporation method using the He gas in the Rh evaporation chamber, connected with the pre-evacuation chamber of Beam Line at Synchrotron Radiation XPS (SR-XPS) enabled this *in-situ* analysis. About samples for evaluation, a practical catalyst will be complicated and the structural factor and its influence for the electronic property are included. Therefore, simplified materials which were precious metal NPs fabricated on the Si wafer coated with oxide thin layer were used as a sample.

Moreover, changing photon energy enables to evaluate not only the adsorption gas but also from Rh surface near the adsorption point to the deeper area near the support material that is based on the practical catalyst. Additionally, the influence

of oxygen for NO adsorption is also studied [14, 32-37]. In the former studies, the behavior of the adsorption gas and Rh surface near the adsorption point were analyzed by Near Ambient Pressure (NAP) XPS. In a NAP system, the pressure of the adsorption gas was about 100 mTorr, for instance. This was far from the practical condition, 760 Torr, and was difficult to regard a same condition as a practical one. On the contrary, in this study, the load lock chamber of the Beam Line was used as a reaction chamber, the behavior of the adsorption gas could be evaluated at 760 Torr without ambient atmosphere.

1.4.2   Computational modeling and calculation for characterization

Knowledge of the atomic structure, that is the surface composition and geometry, is indispensable for analyzing and understanding the electronic property and the mechanism for each reaction. In this respect, the experimental techniques of ultrahigh-vacuum (UHV) have significantly helped our understanding of surface science. However, the clarification for the mechanism cannot be accomplished by this experimental investigation alone. Theoretical calculations are also powerful tools for clarification of the mechanism, because it provides detailed information about the behavior of electrons and the resulting interactions, reaction kinetics as well as the thermodynamics of the reactants, products, intermediates and

transition states. Modern electronic structure theory methods like density-functional theory (DFT) have matured to a standard tool. These techniques are referred to as first-principle to indicate that they do not rely on empirical or fitted parameters and obtain the physical property based on the elements consisted of a molecule or a crystal and its structure. That is to say, physical properties can be predicted by the electronic state calculations [38-40]. In this study, computational modeling and calculations are carried out to provide the thermodynamic and kinetic properties for theoretical insights by DFT.

1.5   Purpose of this thesis

As the first step of MBR for more effective catalyst development, mechanism of NO adsorption–desorption behavior" and the relationship between NO adsorption-desorption behavior and the electronic property of Rh used for active sites are clarified.

The first chapter shows the result of the characterization for Rh NP itself. Rh NPs have been fabricated by the evaporation method using the He gas in the Rh evaporation chamber, connected with the pre-evacuation chamber of BL6N1 at Aichi Synchrotron Radiation Center (Aichi SR). The electronic and geometric properties of the Rh NPs have been verified without atmosphere exposure (in-situ XPS) and after

atmosphere exposure (ex-situ XPS) using SR-XPS and TEM.

The second chapter shows the result of the characterization for NO adsorption on Rh NPs. After Rh NPs were deposited with a same method as in chapter 1, Rh NPs were exposed to NO with and without an ambient atmosphere to study the effect of O_2 on the electronic properties of the Rh NPs and the behavior of NO molecules using SR-XPS.

The third chapter shows the influence of the support material for NO adsorption on Rh NPs. After Rh NPs were deposited on a silicon wafer and CeO_2 thin layer on a silicon wafer with a same method as in chapter 1 and were exposed to NO, the influence of the support material for NO adsorption on Rh NPs was verified. Moreover, a combination with theoretical calculations enables to understand the behaviors thermodynamically.

[1] H.C. Frey, J. AIR & WASTE MANAGEMENT ASSOCIATION **68**, 6, 514 (2018).

[2] J. Woodcock, D. Banister, P. Edwards, A.M Prentice and I. Roberts, Series/Energy and Health 3, 370, 9592, 1078 (2007).

[3] R.N. Colvile, E.J. Hutchinson, J.S. Mindell and R.F. Warren, Atmospheric

Environment **35,** 1537 (2001).

[4] 環境省資料　2016 年度温室効果ガス排出量の算定結果

[5] 石井　素、　J. JIME 47, 6 (2012)

[6] 環境省資料　COP21 の成果と今後

[7] G. C. Koltsakis and A. M. Stamatelos, Prog. Ener. Combu. Sci. **23**, 1 (1997).

[8] H. S. Gandhi, G. W. Graham and R.W. McCabe, J. Catal., **216**, 433 (2003).

[9] R. M. Heck and R. J. Farrauto, Applied Catalysis A: General, **221** 443 (2001).

[10] R.H. Thring, "Homogeneous-Charge Compression-Ignition (HCCI) Engine",
SAE Paper 892068 (1989).

[11] 畑村耕一, HCCI（予混合圧縮着火）ガソリンエンジンの可能性と課題,
Transactions of Society of Automotive Engineers of Japan, **36**, 2 (2005).

[12] H. Muraki, and G. Zhang, Catal. Today, **63**, 337 (2000).

[13] Q. Zheng, R. Farrauto, M.Deeba, and I. Valsamakis, Catalysts, **5**, 1770 (2015).

[14] F. Deushi, A. Ishikawa and H. Nakai, J. Phys. Chem. C, **121**, 15272 (2017).

[15] T. Torimoto, H. Nishiyama, T. Sakata, H. Mori and H. Yoneyama, J.
Electrochem. Soc. **145**, 6, 1964 (1998).

[16] M. Vallden, X.Lai, and D.W. Goodman, Science, **281,** 1647 (1998).

[17] M. Haruta, S. Tsubota, T. Kobayashi, H. Kageyama, M.J. Genet, and B. Delmon,

J. Catal., **144**, 175 (1993).

[18] I. Lopez-Salido, D.C. Lim, and Y.D. Kim, Surf. Science, **588**, 6 (2005).

[19] D.C. Lim, I. Lopez-Salido, and Y.D. Kim, Surf. Science, **598**, 96 (2005).

[20] 松本　健俊、表面科学, 27, 6 314 (2006).

[21] I. Ro, J. Resasco and P. Christopher, ACS Catalysis, **8**, 7368 (2018).

[22] C. T. Campbell, Science, **306**, 234 (2004).

[23] A. Sanchez, S. Abbet, U. Heiz, W.-D. Schneider, H. Hakkinen, R. N. Barnett and Uzi Landman, J. Phys. Chem. A, **103**, 9573 (1999).

[24] J. Guzman and B. C. Gates, J. Phys. Chem. B, **106**, 7695 (2002).

[25] T. Q. Nguyen, M. C. S. Escano, H. Nakanishi, H. Kasai, H. Maekawa, K. Osumi and K. Sato, Applied Surface Science, **288**, 244 (2014).

[26] F. R. Negreiros and S. Fabris, J. Phys. Chem. C 2014, **118**, 21014 (2014).

[27] L. O. Paz-Borbon, A. Lopez-Martinez, I. L. Garzon, A. Posada-Amatillas and H. Gronbeck, Phys. Chem.Chem. Phys., 19, 17845 (2017).

[28] X. Shi and D. Sholl, J. Phys. Chem. C, 116, 10623 (2012).

[29] H. Kawabata, Y. Koda, H. Sumida, M. Shigetsu, A. Takami and K. Inumaru, Chem. Commun. **49**, 4015 (2014).

[30] H. Kawabata, Y. Koda, H. Sumida, M. Shigetsu, A. Takami and K. Inumaru,

Catal. Sci. Technol. **4**, 697 (2014).

[31] S. Blomberg, R. Westerstrom, N. M. Martin, E. Lundgren, J. N. Andersen, M. E. Messing and J. Gustafson, Surf. Science, **628**, 153 (2014).

[32] K. Ueda, K. Isegawa, K. Amemiya, K. Mase and H. Kondoh, ACS Catal., **8**, 11663 (2018).

[33] R. Toyoshima, M. Yoshida, Y. Monya, K. Suzuki, K. Amemiya, K. Mase, B. S. Mun and H. Kondoh, J. Phys. Chem. C **119**, 3033 (2015).

[34] D. Loffreda, D. Simon and P. Sautet, Chem, Phys. Lett. **291**, 15 (1998).

[35] D. Liao, K. M. Glassford, R. Ramprasad and J. B. Adams, Surf. Science, 415, 11 (1998).

[36] C. Popa, A. P. van Bavel, R. A. van Santen, C. F. J. Flipse and A. P. J. Jansen, Surf. Sience, **602**, 2189 (2008).

[37] D. Loffreda, D. Simon and P. Sautet, J. Chem. Phys., **108**, 6447 (1998).

[38] J. Rogal and K. Reuter, Educational Notes RTO-EN-AVT-142, Paper 2.Neuilly-sur-Seine, France: RTO (2007).

[39] 豊浦　和明、J. MMIJ, 129, 270 (2013).

[40] 川添　良幸、Materia, 37, 7, 583 (1998).

Chapter 2

Experimental

Chapter 2: Experimental

2.1 Sample preparation

Rh nanoparticles (NPs) were fabricated by gas evaporation method [1,2]. Fig.2-1 shows the schematic view of the Rh NPs fabrication. This equipment consists of 2 chambers, "Forming chamber" and "Deposition chamber", and 2 chambers are connected with 1/8 inch pipe of stainless. Rh twisted pair wire was used as the evaporation source and was introduced in the forming chamber. After all this equipment were evacuated by the rotary pump or turbo molecular pump, evacuation for the forming chamber stopped and He gas was introduced. Rh wire was charged and then evaporated. When evaporated Rh atoms crushed on He atoms, they were cooled and agglomerated to form nanoparticles. As the deposition chamber was evaporated, the formed NPs are transformed by He gas to the evaporation chamber through the 1/8 inch pipe because of the difference of pressure between 2 chambers. And the evaporated Rh NPs were fabricated on the Si wafer set near the exit of the pipe. Fig.2-2 shows the fabrication equipment in HiSOR.
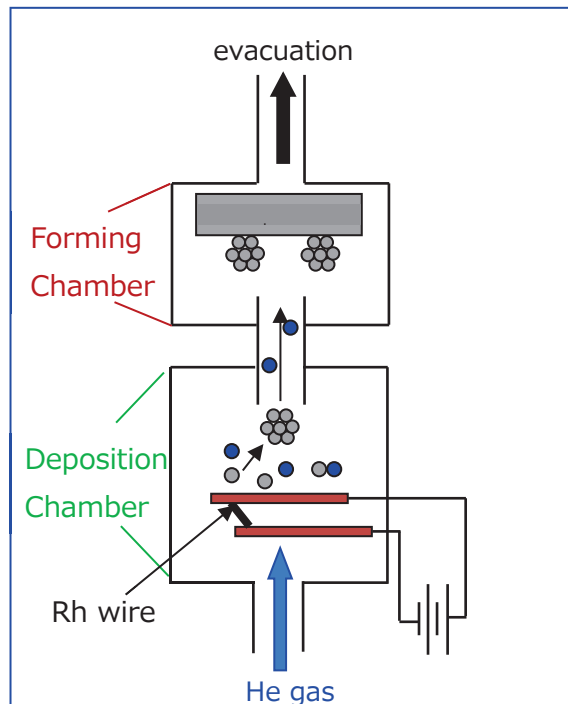
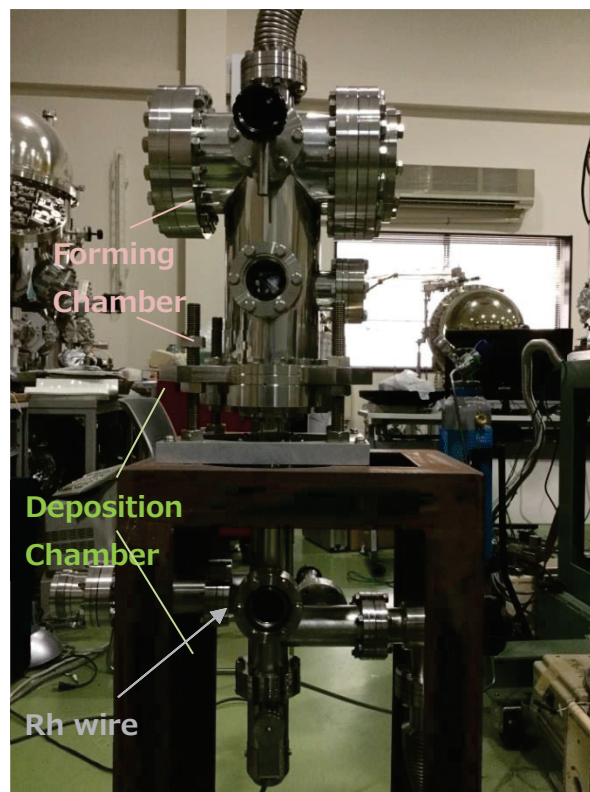Fig.2-1. Schematic view of chamber of fabrication chamber.

Fig.2-2. Fabrication equipment in HiSOR.

2.2　Characterization

2.2.1　X-ray photoelectron spectroscopy (XPS)

2.2.1.1　Principle [3,4]

X-ray photoelectron spectroscopy refers to experimental manipulations based on the photoelectric effect. Fig. 2-3 illustrates the principle of the XPS experiment. The photon impacts on the sample (photoemissive material) and an electron is exited and escapes to the vacuum by the photoelectric effects. The following equation holds.

$$E_B = h\omega - E_k - \phi$$

, where $h\omega$ stands for the energy of the irradiated X-ray, E_B stands for the binding energy of the escaping photoelectron in a sample calibrated at Fermi level,
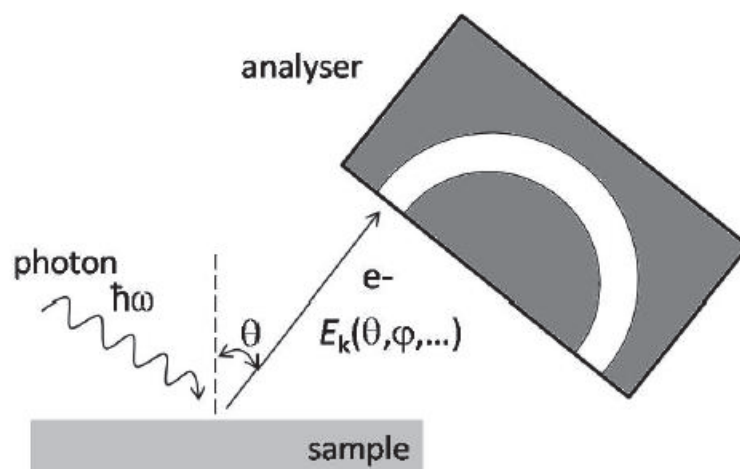

Fig.2-3. Schematic view of the principle of the XPS experiment. The analyzer determines the energy and momentum of the charged particle using several methods depending on the instrument.

the kinetic energy of the photoelectron stands for E_k and the work function of the

energy analyzer stands for ϕ. Fig.2-4 shows a schematic display of the relation

between the energy levels in a solid and the photoelectron energy distribution for

a fixed photon energy $h\omega$. Fermi level is at the highest occupied energy level of

the band and taken to have E_B =0 and kinetic energy measured from the vacuum

level. An actual energy distribution of the photoelectrons would be usually

proportional to the electron energy distribution in the solid, so-called the density
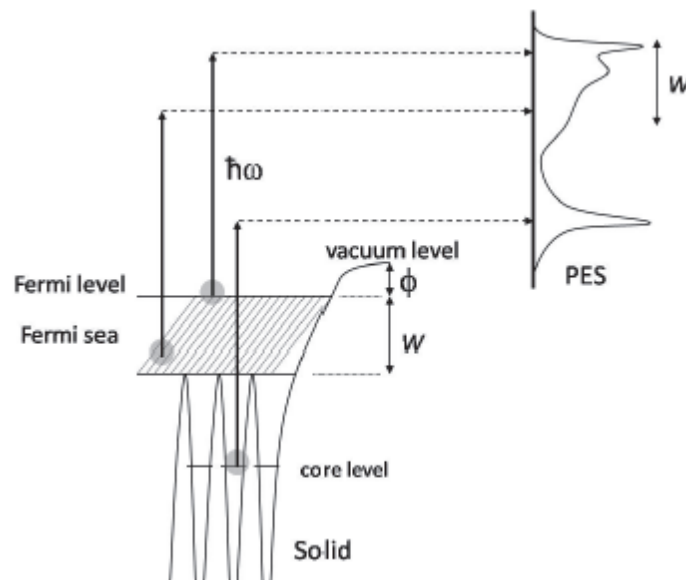
of the states (DOS).

Fig.2-4. XPS from a metallic surface: a schematic plot of the energy levels in
a solid vs the photoelectron energy distribution for a photon of energy h ν .

The binding energy is determined by the element and the electron level, but it

varies depending on the chemical environment around atoms. This is used to

identify the type and chemical state of the element. The mean free path is given as

a function of its kinetic energy, as shown in Fig.2-5. Changing the photon energy
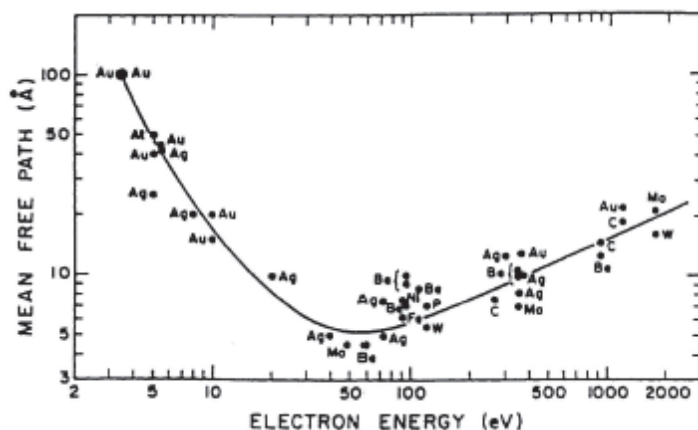

Fig.2-5. Universal curve for the mean free path with respect to the electron kinetic energy [3].

enables to change the escape depth of photonelectrons of the material.

2.2.1.2   Synchrotron Radiation(SR)- XPS [5]

In this study, chemical states of the Rh NP have been investigated by SR-XPS at

BL6N1 in Aichi Synchrotron Radiation Center (AichiSR). Its accumulated

electron energy is 1.2 GeV, accumulated current is 300 mA and perimeter is 72 m.

Fig.2-6 shows a layout of AichiSR and its photon spectrum in Fig.2-7. The

BL6N1 is for soft X-ray XAFS and XPS. Fig.2-8 shows a schematic view of

BL6N1. XPS can be performed with the photon energy from 1.75 keV to 5 keV

(Fig.2-9). Therefore, , to characterize the electronic property in the depth direction,

XPS analysis with SR were adopted because its phton energy is able to change.
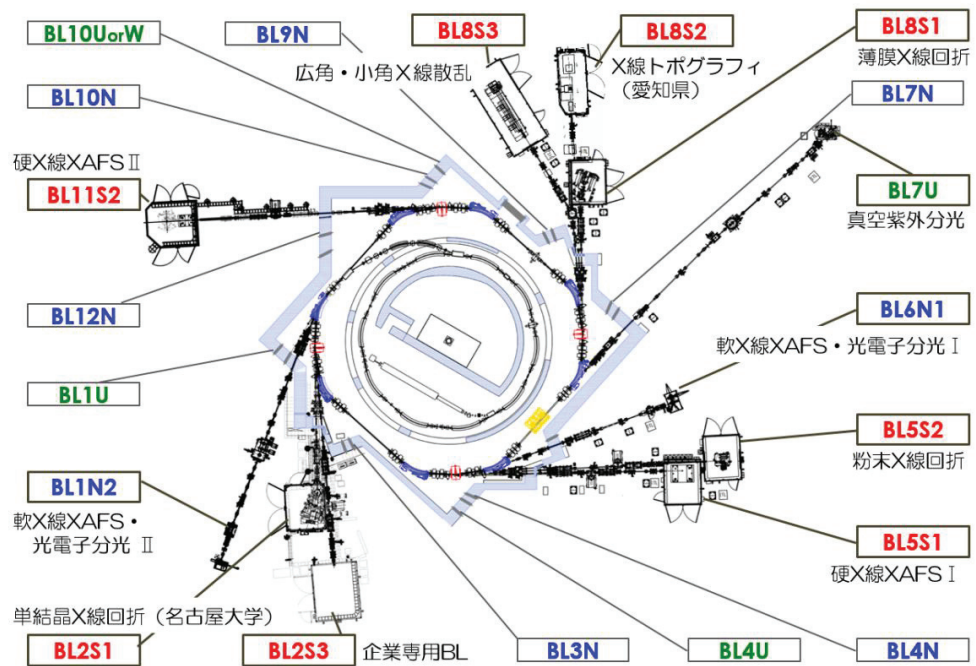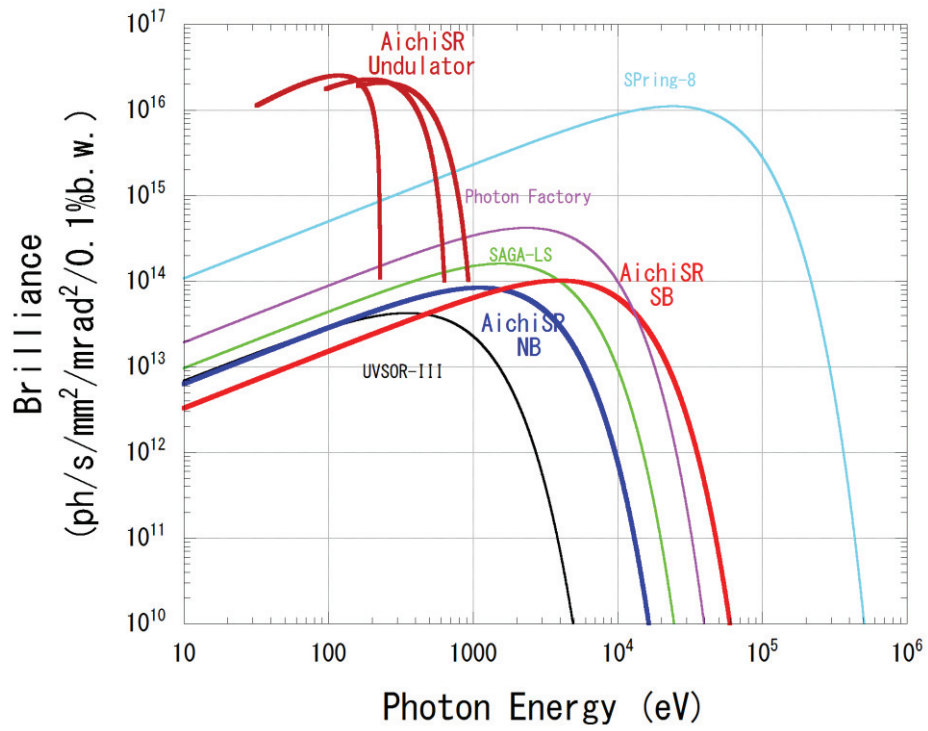

Fig.2-6. The layout of AichiSR.
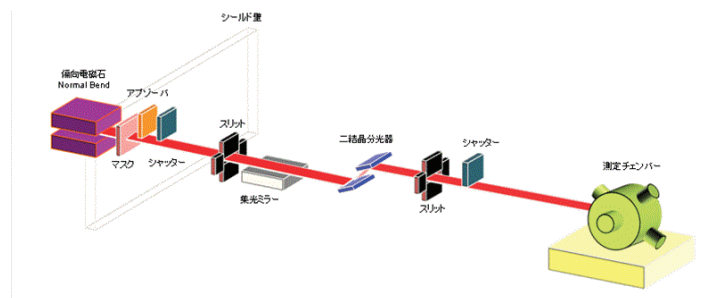
Fig.2-7. The photon spectrum of AichiSR.

Fig.2-8. The schematic view of AichiSR BL6N1.
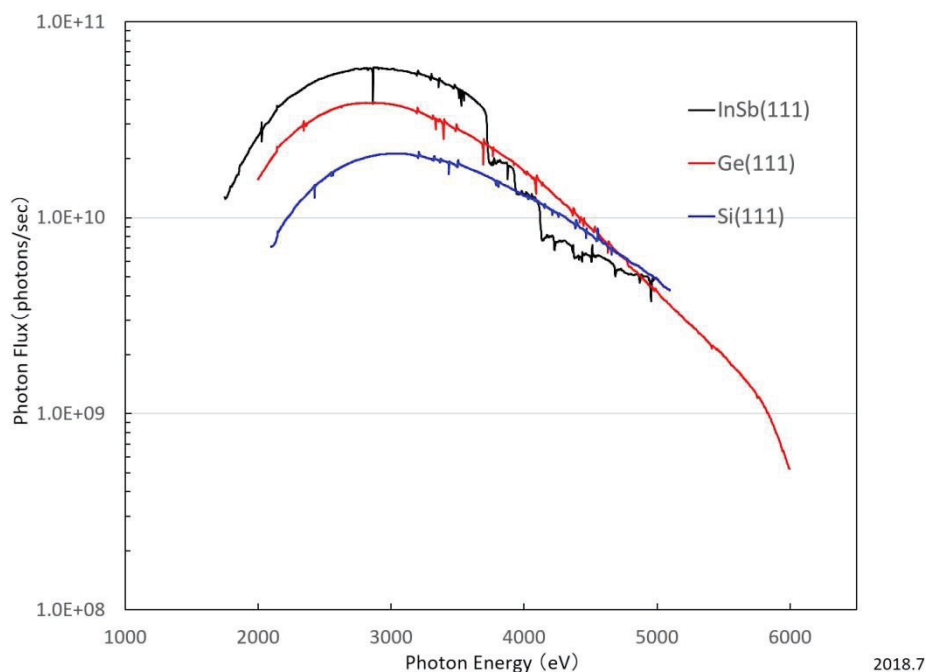
Fig.2-9. The photon flux of AichiSR BL6N1.

2.2.1.3 *in-situ* XPS analysis [5]

NPs fabricated by gas evaporation method are oxidized due to atmosphere exposure. Our first concern is intrinsic property of Rh NPs. For this characterization of the electronic property, *in-situ* XPS is the suitable analytical method because it can exclude the effect of any adsorbed species including oxygen.

Because BL6N1 has a load-lock chamber and a sample transfer system, the evaporation chamber for Rh NPs was connected to the load-lock chamber of the endstation and Rh NP could be able to be analyzed without exposure to ambient

air (Fig.2-10).
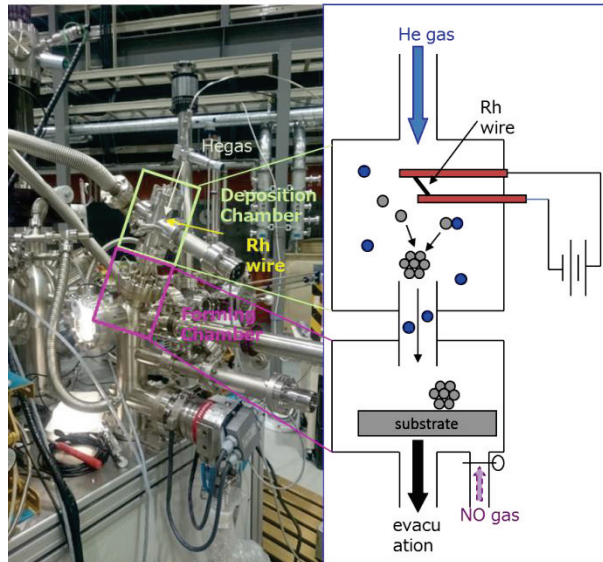
Fig.2-10. The end station at Aichi SR and schematic view of chamber of fabrication chamber.

2.2.2 Transmission electron microscopy (TEM)

2.2.2.1 Principle [6]

Transmission electron microscopy is an observation technique that the accelerated electrons pass through the electronic lens and irradiate to specimen thinned to 100 nm or less and transmitted electrons are magnified and projected onto a fluorescent screen or CCD camera. And it realizes filming images smoothly for a wide range of magnifications from tens of microns (observation over the entire part of cells) to sub nanometer size (observation for the atomic arrangement).

Contrast is due to dispersion and diffraction of the electron beam, and mainly TEM observation provides the fine structural information, moreover, the information about dislocation, stacking fault, particle diameter and so on as well. In addition, by the change of the observation mode, the electon diffraction pattern is able to be obtained to get information about the crystal structureand the crystallinity (Fig.2-11).

2.2.2.2   Procesure of TEM observation

In this study, the particle diameter of Rh nanoparticles were evaluated by TEM using JEOL JEM-3000F with accelarated voltage 300kV at Hiroshima Prefectural Technology Research Institute (Fig.2-12). Rh NPs were fabricated for a short time on a TEM grid for evaluation.
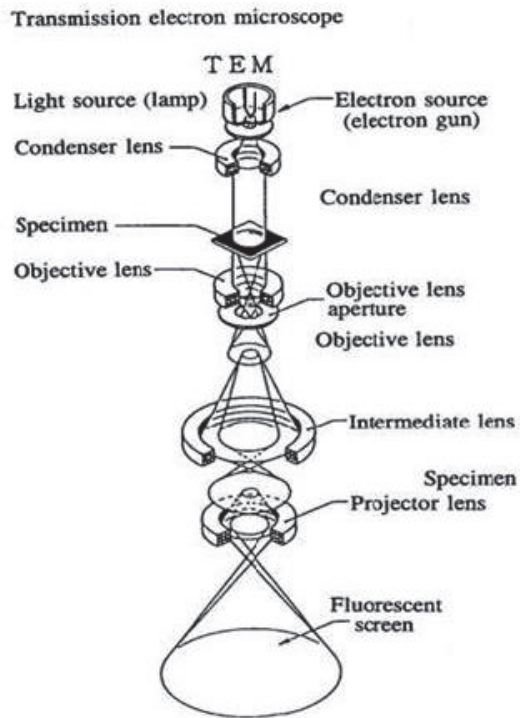
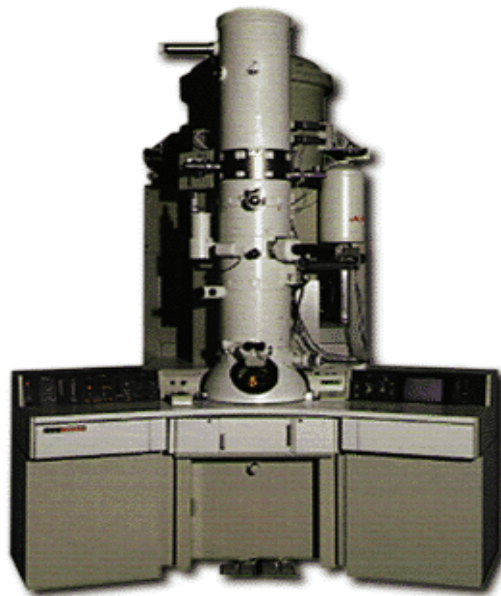Fig.2-11. General layout of a TEM describing the path of electron beam in a TEM [6].

Fig.2-12. JEM-3000F at Hiroshima Prefectural Technology Research Institute [8].
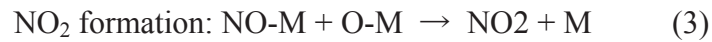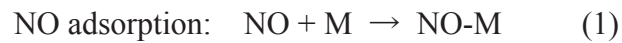
2.3 Computational modeling and calculation for characterization

Electronic structure calculations were performed within a density functional theory (DFT) method, using Dmol^3 in Material Studio (version 7) of Accelrys Inc.. In the DMol^3 methods, the physical wave functions are expanded in terms of accurate numerical basis sets. I used the double-numeric quality basis set with polarization functions (DNP). Perdew-Burke-Ernzerhof exchange correlation functional with revised parameters (RPBE functional) was employed as the the gradient-corrected GGA functional. A Fermi smearing of 0.002 hartree (1 hartree = 27.2114 eV) and a real-space cutoff of 4Å were used to improve computationap performance. Periodic surface slabs of four layers' thickness were used, with a 15Å of vacuum region between the slabs. Adsorbate and the two top layers of metal were allowed to relax in all the geometry optimization calculations without symmetry restriction. The tolerances of energy, gradient, and displacement convergence were 2×10^{-5} hartree, 4×10^{-3} hartree/Å, and $5\times10^{-3}\text{Å}$, respectively. The maximum gradient for most of the optimized structures was less than 2×10^{-3} hartree/Å.

The slab model of CeO_2 was cut from the bulk cubic (*Fm3m*) CaF_2-like structure using the optimized parameter a_0 of 5.526 Å, in good agreement with reference a_0 of 5.40Å. The slab model of SiO2 was cut from the bulk alpha-quartz SiO_2 structure

using the optimized parameter a_0 and b_0 of $5.069\,\text{Å}$ and c_0 of $5.572\,\text{Å}$, in good agreement with reference a_0 and b_0 of $4.9137\,\text{Å}$ and c_0 of $5.4047\,\text{Å}$.

I focused on the following three reactions (eq 1-3), which constitute the key elementary steps

$$\text{NO adsorption:} \quad \text{NO} + \text{M} \rightarrow \text{NO-M} \qquad (1)$$

$$\text{NO dissociation: NO-M} \rightarrow \text{N-, O-M} \qquad (2)$$

$$\text{NO}_2 \text{ formation: NO-M} + \text{O-M} \rightarrow \text{NO2} + \text{M} \qquad (3)$$

The adsorption energy (E_{ad}) for an adsorbate A was calculated using the equation

$$E_{ad} = E(\text{surf} -A) - [E(\text{surf}) + E(A)] \qquad (4)$$

Where $E(\text{surf} -A)$, $E(A)$ and $E(\text{surf})$ are the electronic energy contributions from the surface –adsorbate system, the adsorbate and the surface, respectively. According to this definition, negetive E_{ad} corresponds to stable adsorption on the surface.

[1] H. Niwa, S. Ogawa, K. Nakanishi, G. Kutluk, T. Ohta, and S. Yagi, J. Surf. Anal. 17, 278 (2011).

[2] 小田　正明、表面科学、第 8 巻第 5 号 335 (1987).

[3] J. D. Lee, J. Surf. Anal.　16, 42 (2009).

[4] K. Yoshihara, J. Vac. Soc. Jpn. 56, 4, 37 (2013).

[5] あいちシンクロトン放射光センターホームページ、https://www.astf-kha.jp/

[6] 進藤　大輔、及川　哲夫、材料評価のための分析顕微鏡法 (1995)、共立出版（株）

[7] JEOL 2000FX Handbook.

[8] https://www.pref.hiroshima.lg.jp/soshiki/28/a501.html.

Chapter 3

Fabrication and in/ex–situ XPS characterization of Rh nanoparticles

Chapter 3 Fabrication and in/ex–situ XPS characterization of Rh nanoparticles

3.1 Introduction

To meet the present stringent regulation for automobile emission, catalysts play an important role in purifying exhaust gases. For NO reduction, rhodium (Rh) is the essential precious metal as the active site [1-3]. To make Rh more effective for NO reduction, Rh particle must be as small as it can be to increase the number of reaction site. As the metal particle size decreases below 10 nm, both different electronic and geometric properties can be observed in comparison with those of the bulk material [4-7].

Our first concern is the intrinsic properties of Rh nanoparticles. For this characterization of the electronic property, in-situ X-ray photoelectron spectroscopy (XPS) is the suitable analytical method, excluding the influence of any adsorbed components. On the other side, catalysts for purifying the exhaust gases are used under atmosphere. Therefore, our second concern is the properties of nanoparticles in practical use condition. Ex-situ XPS, that is XPS analysis after atmosphere exposure,

clarifies this issue. In the process of NO reduction, NO molecules adsorb on the metallic Rh surface. Under atmosphere, Rh oxide layer is on the surface of Rh particle and the thickness of the oxide layer influences its performance [8-10]. In the case of XPS analysis in laboratory, using Al Kα radiation (1486.6 eV), *calculated inelastic mean free path of Rh is* 1.9 nm [11], less than or equal to about one Rh oxide layer. In the case of XPS analysis in Synchrotron radiation (SR), increasing a photon energy enables the inelastic mean free path to increase. In this paper, XPS analysis with SR is adopted to characterize the electronic property of Rh nanoparticle in the depth direction.

The purpose of this paper is to reveal the geometric and electronic properties of Rh nanoparticles by using both TEM and in/ex-situ XPS with SR.

3.2.2 Analysis of Rh nanoparticle

TEM experiments were carried out using JEOL JEM-3000F, accelarating energy at 300 kV. To evaluate the size of Rh nanoparticles, another sample of the TEM grid with a short time fabrication was prepared.

Chemical states of the Rh nanoparticle were investigated by XPS at BL6N1 in Aichi Synchrotron Radiation Center. As the evaporation chamber for Rh nanoparticles was

connected with the pre-evacuation chamber of the endstation, Rh nanoparticle was able to be analyzed without atmosphere exposure. A photon energy for XPS analysis was set at 2.0 keV or 3.5 keV. The spectra were calibrated by the peak position of Au $4f_{7/2}$ (83.95 eV). The binding energies of $Rh3d_{5/2}$ for metallic Rh, Rh_2O_3 and RhO_2 are set at 307.2 eV, 308.2 eV and 309.5 eV, respectively [12-14]. The deconvolution analysis of the $Rh3d_{5/2}$ peaks was performed by CASA XPS [15] and each area of the Rh component with a different oxidation state were calculated as the existing ratio. In/ex-situ XPS conditions are 3 patterns; (a) Rh nanoparticles without atmosphere exposure (in-situ XPS) (b) air exposed for 10 minutes (c) air exposed for a month.

3.3 Results and Discussions

3.3.1 TEM studies of Rh nanoparticle

TEM image of the Rh nanoparticles deposited with the same condition as the XPS sample shows in Figure 3-1. Rh nanoparticles have spherical shape and were deposited with the structural property of nanoparticles indicating Rh didn't form the agglomerate. Using Figure 3-2, the size of Rh nanoparticles was evaluated and the size distribution of the Rh nanoparticles is also shown in Figure 3-3. The diameter of the Rh nanoparticles is in the region about 1-3.5 nm in diameter. The estimated

average size and standard deviation (S.D.) are 1.8±0.5 nm.
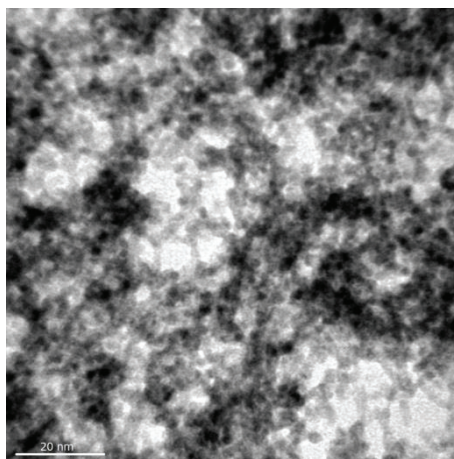

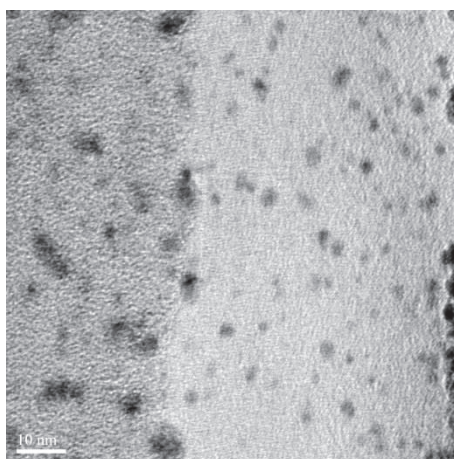Fig.3-1.　TEM image of Rh nanoparticles.

Fig.3-2.　TEM image of Rh nanoparticles for the evaluation of the size of Rh
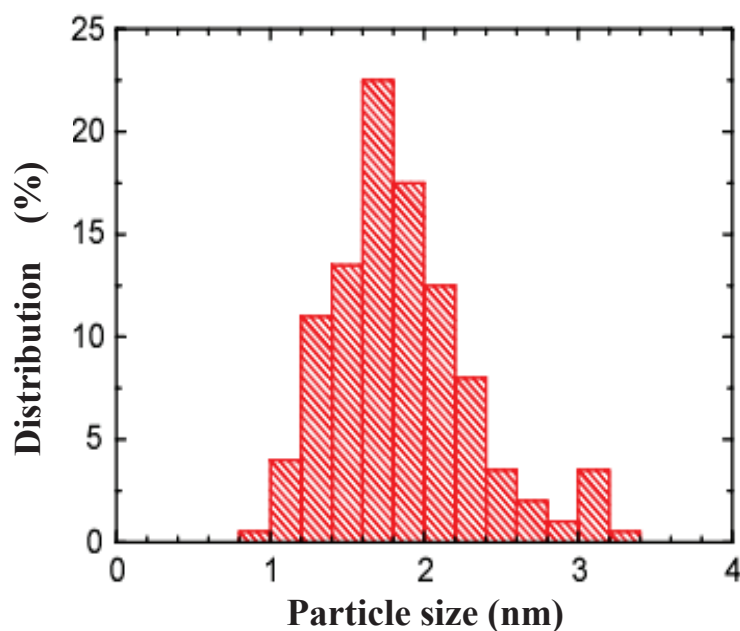
nanoparticles.

Fig.3-3.   Size distribution of Rh nanoparticles.

3.3.2 XPS analysis

From the in-situ XPS survey spectrum of Rh nanoparticles for (a) with the photon

energy of 2.0 keV, not shown in here, the peaks of Rh3d, Rh3p and valence band

can be found. The peaks of O1s and C1s cannot be found. It means that the

nanoparticles without atmosphere exposure are metallic state and no

contaminations. Also the peaks of the substrate silicon cannot be detected. This

and TEM results indicate that the Rh nanoparticle is deposited like a thin film and

in this paper, this is called 'Rh nanoparticles'. From the ex-situ XPS survey

spectra, Rh nanoparticles for (c) have the peaks of Rh3d, Rh3p, valence band, O1s

derived from Rh oxides and C1s derived from contaminations. It indicates that the

Rh oxides exist on the surface of the Rh nanoparticles. Rh nanoparticles for (b) have the small peaks of O1s and C1s. It indicates that even a small amount of O_2 changes the surface to Rh oxides.

Figure 3-4 shows the $Rh3d_{5/2}$ and $Rh3d_{3/2}$ spectra of three samples (a)-(c) measured by 2.0 keV XPS and the components analysis is summarized from Table 3-1 to Table 3-3. The peak top of Rh nanoparticles in the case of in-situ XPS of $Rh3d_{5/2}$ for (a) is at 307.4 eV. Judging from the result of the deconvolution analysis, Rh nanoparticles are in a metallic state. However, in the case of ex-situ XPS for (b), the peak top is at 307.5 eV with a shoulder at 308.5 eV including 17 % of Rh_2O_3. These results indicate that the part of the Rh surface changes to Rh oxides by atmosphere exposure even for a short time. Moreover, in the case of ex-situ XPS for (c), the peak top is at 309.5 eV. The result of the deconvolution analysis indicates that 37 % of Rh_2O_3, 38 % of RhO_2 whose $3d_{5/2}$ peak position is 309.2 eV and 13 % of Rh metal exist. This suggests that long time atmosphere exposure proceeds some Rh oxidations. Moreover, the peak with lower binding energy than that of Rh metal is also observed. One possibility of Rh state with lower binding energy might be the formation of hydrides compounds, reacting with H_2O in the air [16, 17]. We will confirm it by the experiment of pure O_2

exposure with Rh nanoparticles whether this Rh compound will be formed or not

near future.
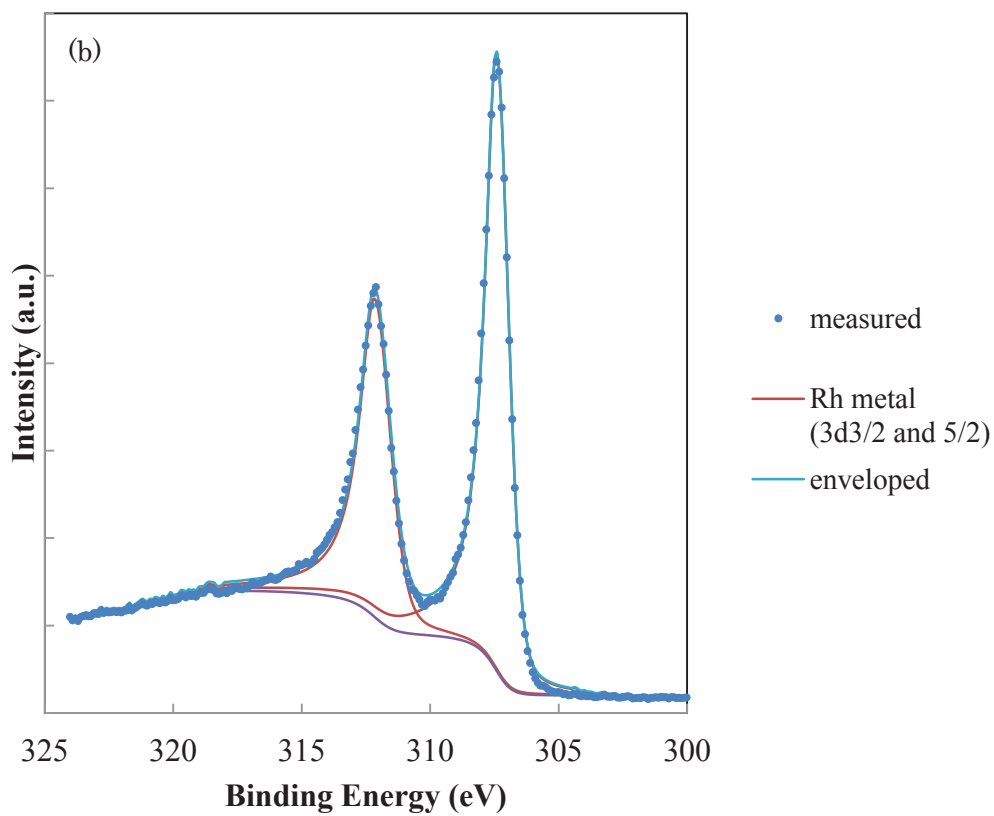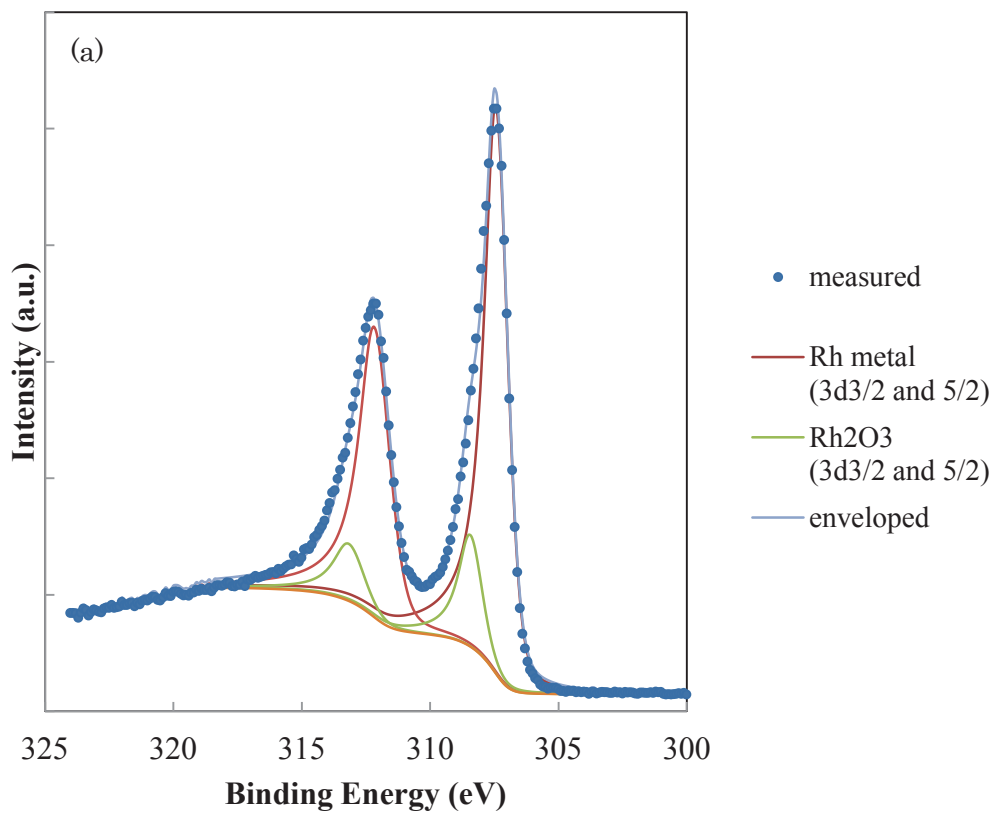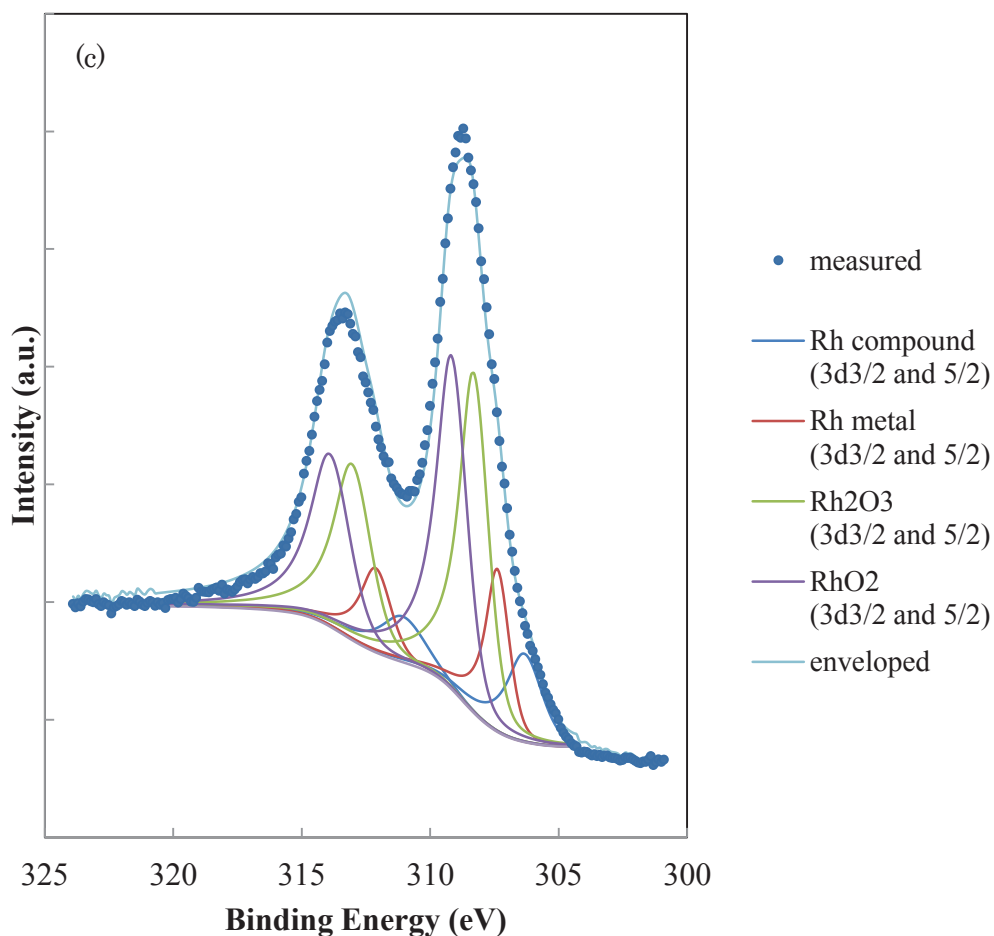
Fig.3-4.   Result of the deconvolution analysis of Rh3d spectra at 2.0 keV.
（a）in-situ XPS (b) ex-situ XPS exposure for 10 minutes (c) ex-situ XPS exposure for a month.

Table 3-1: Result of the deconvolution analysis of Rh3d$_{5/2}$ of (a) in-situ XPS analysis at 2.0 keV.

Spectrum	Position（eV)	Existing ratio(%)
Rh metal	307.4	100

Table 3-2: Result of the deconvolution analysis of Rh3d$_{5/2}$ of (b) ex-situ XPS analysis exposure for 10 minutes at 2.0 keV.

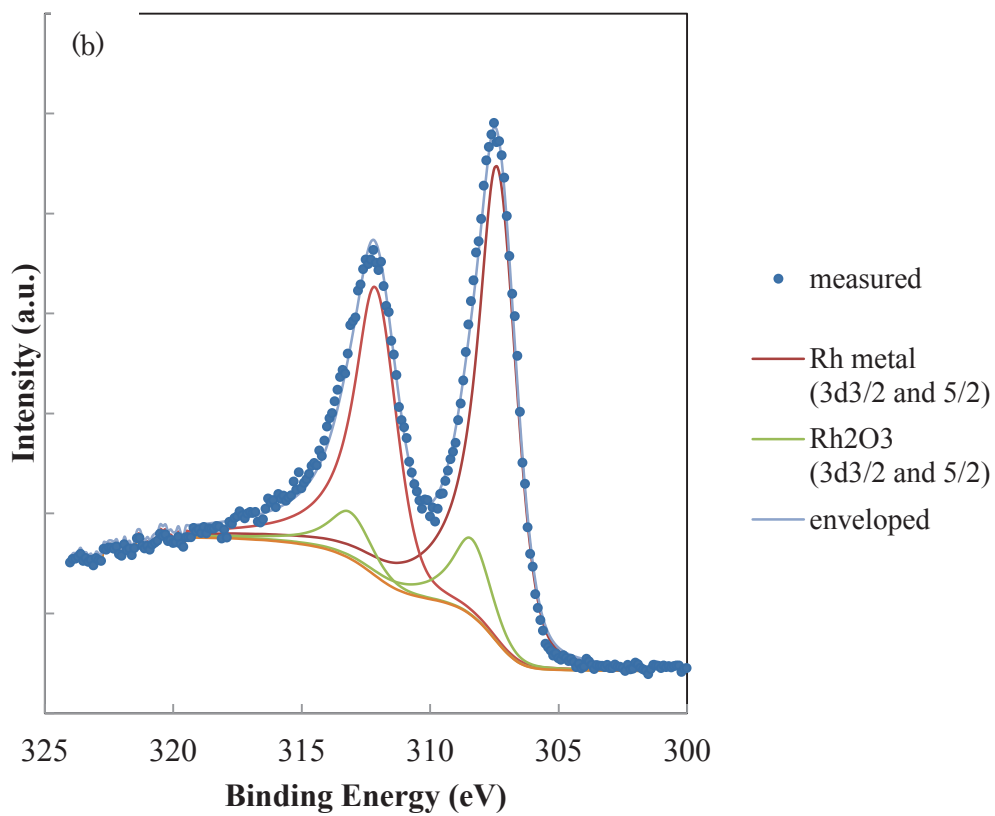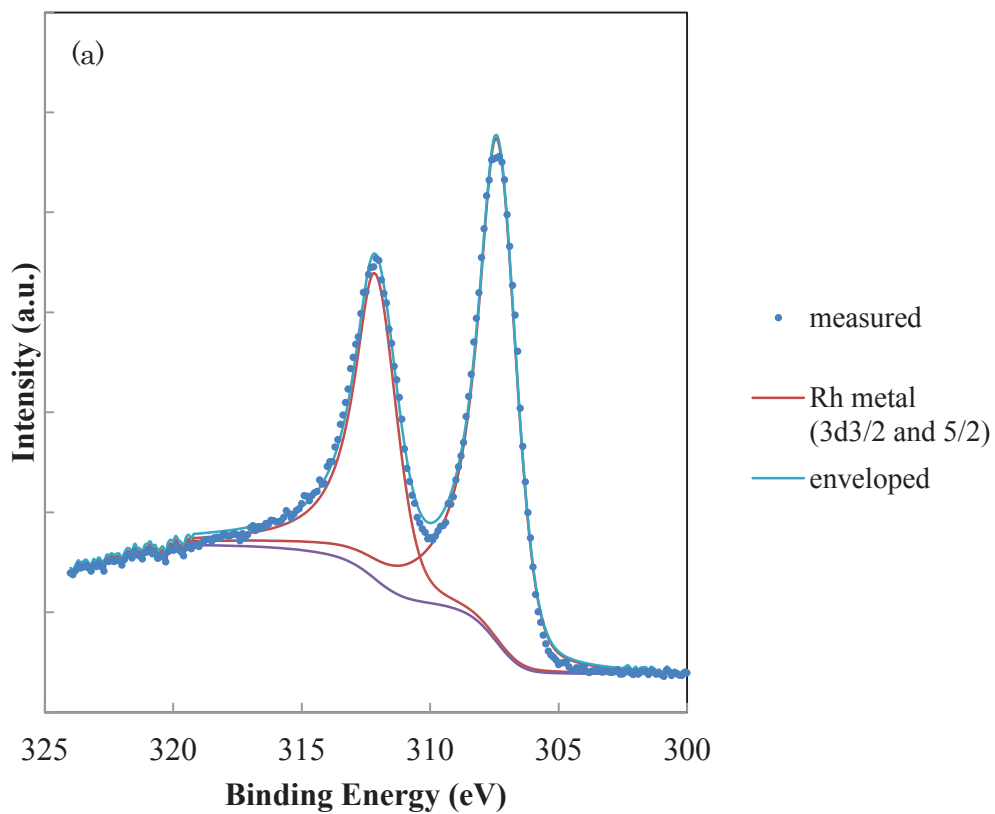| Spectrum	Position（eV)	Existing ratio(%)
Rh metal	307.5	83
Rh$_2$O$_3$	308.5	17

Table 3-3: Result of the deconvolution analysis of $3d_{5/2}$ of (c) ex-situ XPS analysis exposure for a month at 2.0 keV.

Spectrum	Position	Existing ratio(%)
Rh compound	306.4	12
Rh metal	307.4	13
Rh_2O_3	308.3	37
RhO_2	309.2	38

Subsequently, the electronic properties of Rh nanoparticles in the depth direction of the thin layer are verified by using the photon energy at 3.5 keV. Figure 3-5 shows the Rh3d of three samples (a)-(c) measured by 3.5 keV XPS and the components analysis is summarized from Table 3-4 to Table 3-6. The calculated inelastic mean free path of Rh at 2.0 keV or 3.5 keV is 2.4 nm or 3.7 nm [11], respectively. The peak top position and the shape of Rh3d spectrum of Rh nanoparticles in the case of in-situ XPS for (a) is the same as with 2.0 keV. This indicates that metallic Rh exists in depth region within the mean free path of 3.7 nm for 3.5 keV.

From the result of the deconvolution analysis in the case of ex-situ XPS for (b) with 2 keV, metallic Rh and Rh_2O_3 exist as 83 % and 17 %, respectively (Table 2). Table 3-5 shows the metallic Rh component increases to 87 %. Because the higher photon energy enables to detect the deeper region of Rh nanoparticles, the metallic component in the deeper region add to the spectrum. This indicates that

51

the outermost surface of the layer of Rh nanoparticles is Rh_2O_3. On the other hand, the peak top positions in the case of ex-situ XPS for (c) with 3.5 keV shift to the higher binding energy than the Rh3d spectrum with 2.0 keV. In the comparison between 2.0 keV and 3.5 keV spectra for (c) (see in Table 3-3 and Table 3-6) the oxide components of Rh3d spectra at the higher binding energy than that of metallic states increase 75 % to 81 %. And Rh spectrum with the higher binding energy (310.2 eV) than that of RhO_2 assigned in Table 6 can be found. In general, the positive core level shift attributes to the particle size effect [6, 7, 13, 18-21] or the metal-support interaction [22, 23] and so on. In this case, the particle size effect is excluded because this behavior cannot be seen at analysis with 2.0 keV. Moreover this result suggests that the Rh oxide increases in the depth direction, and the deep area is in the higher oxidation state. One possibility of this result would be the metal-support effect, as Rh oxidation state with the higher binding energy can exist at Rh on Al_2O_3 after aging with high temperature in air [24, 25]. If a substrate has the oxide layer on its surface, Rh might has the possibility to become the higher oxidation state. We will have the further investigation and characterize this Rh state.
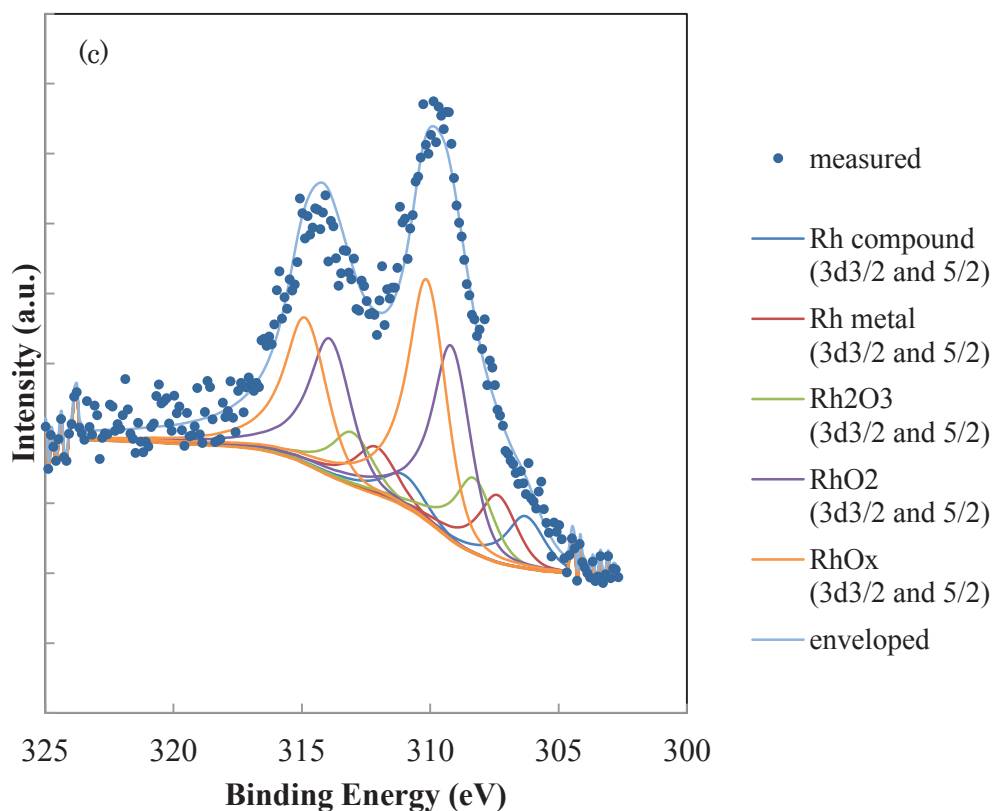
Fig.3-5 Result of the deconvolution analysis of Rh3d spectra.

(a) in-situ XPS (b) ex-situ XPS exposure for 10 minutes (c) ex-situ XPS exposure for a month.

Table 3-4: Result of the deconvolution analysis of Rh3d$_{5/2}$ of (a) in-situ XPS analysis at 3.5 keV.

Spectrum	Position	Existing ratio(%)
Rh metal	307.4	100

Table 3-5: Result of the deconvolution analysis of Rh3d$_{5/2}$ of (b) ex-situ XPS analysis exposure for 10 minutes at 3.5 keV.

Spectrum	Position	Existing ratio(%)
Rh metal	307.4	87
Rh$_2$O$_3$	308.4	13

Table 3-6: Result of the deconvolution analysis of Rh3d$_{5/2}$ of (c) ex-situ XPS analysis exposure for a month at 3.5 keV.

Spectrum	Position	Existing ratio(%)
Rh compound	306.3	9
Rh metal	307.4	10
Rh$_2$O$_3$	308.3	12
RhO$_2$	309.2	31
RhO$_x$	310.2	38

3.4. Conclusions

Rh nanoparticles have been fabricated by the evaporation method. These size are estimated 1.8 ± 0.5 nm in diameter. Judging from the result of the in-situ XPS analysis with SR, the Rh nanoparticles without atmosphere exposure is the Rh metallic state. On the other hand, by the ex-situ XPS analysis, the outermost surface changes into Rh$_2$O$_3$ and RhO$_2$. Changing a photon energy for XPS analysis from 2.0 keV to 3.5 keV enabled to analyze the chemical state in the depth direction.

References

[1] H. Muraki, and G. Zhang, Catal. Today **63**, 337 (2000).

[2] H.S. Gandhi, G.W. Graham, and R.W. McCabe, J. Catal. **216**, 433 (2003).

[3] Q. Zheng, R. Farrauto, M.Deeba, and I. Valsamakis, Catalysts **5**, 1770 (2015).

[4] M. Vallden, X.Lai, and D.W. Goodman, Science **281,** 1647 (1998).

[5] M. Haruta, S. Tsubota, T. Kobayashi, H. Kageyama, M.J. Genet, and B. Delmon, J. Catal. **144**, 175 (1993).

[6] I. Lopez-Salido, D.C. Lim, and Y.D. Kim, Surf. Science **588**, 6 (2005).

[7] D.C. Lim, I. Lopez-Salido, and Y.D. Kim, Surf. Science **598**, 96 (2005).

[8] H. Kawabata, Y. Koda, H. Sumida, M. Shigetsu, A. Takami and K. Inumaru, Chem. Commun. **49**, 4015 (2014).

[9] H. Kawabata, Y. Koda, H. Sumida, M. Shigetsu, A. Takami and K. Inumaru, Catal. Sci. Technol. **4**, 697 (2014).

[10] J. G. Nunan, H. J. Robota, M. J. Cohn and S. A. Bradley, J. Catal. **133**, 309 (1992).

[11] calculated using QUASES-IMFP-TPP2M Ver.3.0. S. Tanuma, C. J. Powell, D. R. Penn, Surf. Interf. Anal. **21**, 165 (1994).

[12] J. F. Moulder, W. F. Stickle, P.E. Sobol and K. D. Bomber, HANDBOOK OF X-RAY SPECTROSCOPY, Perkin Elmer Corporation (1992).

[13] S. Kim, K. Qadir, S. Jin, A. S. Reddy, B. Seo, B. S. Mun, S. H. Joo and J. Y. Park, Catalysis Today **185**, 131 (2012).

[14] M. E. Grass, Y. Zhang, D. R. Butcher, J. Y. Park, Y. Li, H. Bluhm, K. M. Bratlie, T. Zhang and G. A. Somorjai, Angew. Chem. Int. Ed. **47**, 8893 (2008).

[15] http://www.casaxps.com/

[16] S. Ogawa, T. Fujimoto, T. Kanai, N. Uchiyama, C. Tsukada, T. Yoshida, S. Yagi, e-J. Surf. Sci. Nanotech. **13**, 343 (2015).

[17] A.M. Venezia, A. Rossi, D. Duca, A. Martorana, G. De-ganello, Appl. Catal. A: General **125**, 113 (1995).

[18] D. C. Lim, I. Lopez-Salido and Y. D. Kim, Appl. Surf. Sci. **253** 959 (2006).

[19] Radnik, C. Mohr and P. Claus, Phys. Chem. Chem. Phys. **5**, 172 (2003).

[20] P. Zhang and T. K. Sham, Phys. Rev. Lett. **90**, 245502 (2003).

[21] H.-G. Boyen, A. Ethirajan, G. Kästle, F. Weigl, P. Ziemann, G. Schmid, M. G. Garnier, M. Büttner, and P. Oelhafen, Phys. Rev. Lett. **94**, 016804 (2005).

[22] V. Vijayakrishnan, A. Chainani, D. D. Sarma and C. N. R. Rao, J. Phys. Chem. **96**, 8679 (1992).

[23] V. I. Bukhtiyarov, A. F. Carley, L. A. Dollard and M. W. Roberts, Surf. Science **381**, L605 (1997).

[24] K. Dohmae, Y. Hirose, M. Kimura, R&D Review of Toyota CRDL **1**, 75 (1997).

[25] B. Zhao, R. Ran, Y. Cao, X. Wu, D. Weng, J. Fan and X. Wu, Applied Surface Science **308**, 230 (2014).

Chapter 4

Characterization by synchrotron-radiation X-ray photoelectron spectroscopy of NO adsorption on Rh nanoparticles

4.1. Introduction

Catalysts play an important role in purifying exhaust gases to meet the stringent regulations for automobile emissions. From the point of view of fuel efficiency, automobile engines are required to operate under lean condition (high air-to-fuel ratio) which means that maintaining the performance in NO reduction becomes a serious issue. Rhodium is a precious metal that is essential to cutting NO emission by reducing nitrogen oxides to nitrogen and oxygen [1-3], and one way to make Rh more effective in NO reduction is minimizing the Rh particle size to maximize the number of reaction sites. As the metal particle size decreases below 10 nm, electronic and geometric properties that are different from those of the bulk material can be observed [4-7]. Another way to boost NO reduction is exploiting the Rh surface, whose electronic properties are suitable for NO adsorption. Table 4-1 shows my result of the calculation of NO adsorption energy for Rh bulk material and Rh NP. NO adsorption energy of Rh NO is lower than that of Rh bulk material. This means that NO adsorbs on Rh NP easier than Rh bulk material, implying Rh NP is more active. This coincides with the earlier studies [8]. Moreover, NO molecules adsorbed on Rh bulk material stay display no reaction at room temperature, for example, NO dissociation reaction [9,10].

Table 4-1 Result of the calculation of NO adsorption energy.

sample		NO adsorption energy/eV
Rh NP	Rh34 cluster	−2.41
Rh bulk material	Rh(111) 2x2	−2.28

In respond to these results, the first concern regarding effective use of Rh is understanding the intrinsic properties of Rh nanoparticles. *In-situ* X-ray photoelectron spectroscopy (XPS) is a suitable analytical method for characterization of the electronic properties of Rh because it can exclude the effect of any adsorbed species. On the other hand, the catalysts for purification of exhaust gases are used in ambient air. Therefore, the second concern is understanding the properties of nanoparticles under practical application conditions. *Ex-situ* XPS, that is XPS analysis conducted after exposure to atmospheric air, clarifies this issue. In previous studies, a Rh oxide layer was observed on the surface of Rh particles after exposure to ambient air, and the thickness of this oxide layer was found to affect its performance [11-14]. In our previous work, using synchrotron radiation (SR) XPS, we revealed that Rh nanoparticles that were not exposed to ambient air were in the metallic state, but they were oxidized into Rh_2O_3 and RhO_2 on the outermost surface upon exposure to the atmosphere [15].

The purpose of this paper is to report effect of ambient O_2 on the electronic properties of Rh nanoparticles and the behavior of NO molecules using *in-situ* or *ex-*

situ XPS with SR.

4.2. Experimental

4.2.1 Preparation of Rh nanoparticles

Rh nanoparticles were fabricated by the evaporation method [16] in a Rh evaporation chamber. The evaporation chamber was connected to the load-lock chamber of BL6N1 at the Aichi Synchrotron Radiation Center (Aichi SR) in Japan. A Rh wire (4N) was evaporated to release Rh atoms and the Rh nanoparticles were grown under 50 Torr of high-purity He gas (5N5). The nanoparticles were transferred to the deposition chamber through a stainless steel pipe and deposited on a grid and an n-type Si wafer with <100> orientation. The Si wafer had been cleaned by only ultrasonic waves with an ethanol solution. The grid and the Si wafer were set in the depostion chamber as the substrates of the transmission electron microscopy (TEM) and XPS samples, respectively.

4.2.2 Analysis of Rh nanoparticles under different conditions

TEM experiments were carried out using a transmission electron microscope (JEM-3000F, JEOL, Hiroshima Prefectural Technology Research Institute) at an

accelerating voltage of 300 kV. To evaluate the size of the Rh nanoparticles, the

dispersed Rh nanoparticles were deposited on the grid within a short period of time.

The chemical states of the Rh nanoparticles under different conditions were

investigated by SR-XPS at BL6N1 in Aichi SR. The photon energy for XPS

analysis was set at lower enrgy 2.0 keV to evaluate the surface of Rh nanoparticles

which has the NO adsorption point. As the evaporation chamber for Rh

nanoparticles was connected to the load-lock chamber, the Rh nanoparticles could

be analyzed without exposure to ambient air. A NO (2% in He) gas cylinder was

connected to the evaporation chamber and the NO gas was introduced after

deposition of the Rh nanoparticles. X-ray photoelectron spectra were collected for

three different samples of Rh nanoparticles: (a) before exposure to NO; (b) after

exposure to NO for 5 min; (c) after exposure to NO for 5 min in ambient air. The

spectra were calibrated against the peak of Au $4f_{7/2}$ at 83.95 eV [17]. The binding

energies of Rh $3d_{5/2}$ for metallic Rh, Rh_2O_3, and RhO_2 are 307.2, 308.2, and 309.5

eV, respectively [18-20], and the difference between Rh $3d_{5/2}$ and Rh $3d_{3/2}$ is 4.74

eV. The deconvolution analysis of the Rh $3d_{5/2}$ peaks was performed by CASA XPS

[21], and each area of the Rh species with a different oxidation state was estimated

as the fraction of that species in the deposited Rh nanoparticles.

4.3. Results and Discussions

4.3.1 TEM study

The TEM image of the Rh particles in Figure 4-1 shows that particles with spherical shape were deposited. Using Figure 4-1, the size of the Rh particles was evaluated, and the size distribution of the Rh particles is shown in Figure 4-2. The diameter of the Rh particles varied from 1.7 to 4.8 nm, and the estimated average size was 2.7 ± 0.6 nm, where the standard deviation (S.D.) was used for the uncertainty.
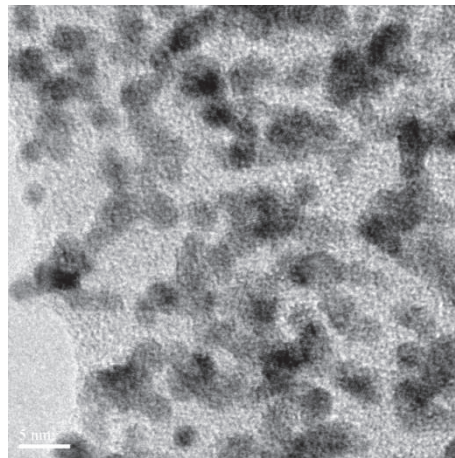

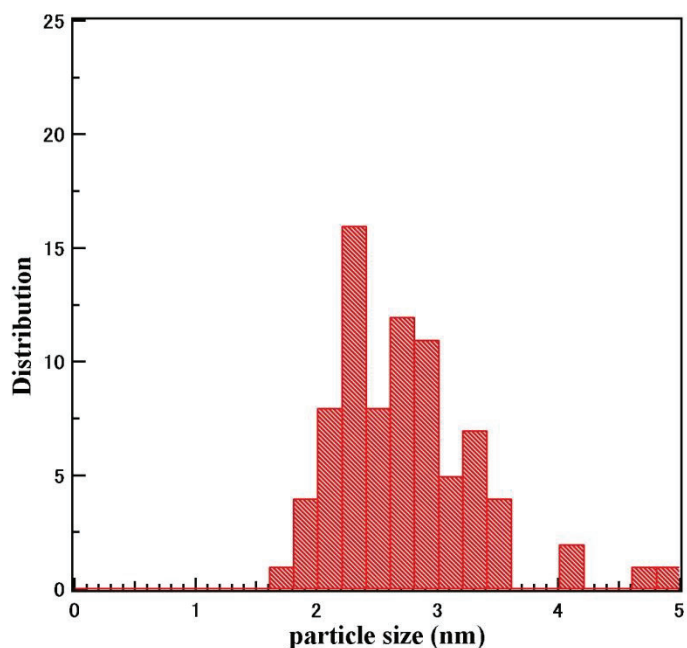Fig.4-1.　TEM image of Rh nanoparticles.

Fig.4-2.   Size distribution of Rh nanoparticles.

4.3.2 XPS analysis

The peaks of Rh 3d and Rh 3p, and the valence band can be found in the *in- situ* XPS survey spectrum of Rh nanoparticles for sample (a), which is not shown here. The peaks of O 1s and C 1s are absent, which means that the nanoparticles that were not exposed to ambient air were in the metallic state and there was no contamination. The peaks of the silicon substrate are also absent. These XPS results and the TEM images indicate that the Rh nanoparticles were deposited like a thin film on the substrate. Here after, the deposited film is referred to as the "Rh nanoparticles".

Figures 4-3 and 4-4 show the Rh 3d and N 1s spectra of sample (a), and the

components corresponding to the Rh $3d_{5/2}$ spectrum are summarized in Table 4-1.

The peak in the Rh $3d_{5/2}$ spectrum of sample (a) is located at 307.3 eV. The

deconvolution analysis indicates that the Rh nanoparticles in sample (a) were in the

metallic state. In the N 1s spectrum, the small peak at 397.5 eV corresponds to

atomic N, which might be related to contaminants [22, 23].

Table 4-1: Result of deconvolution analysis of Rh $3d_{5/2}$ spectrum of sample (a) before
exposure to NO.

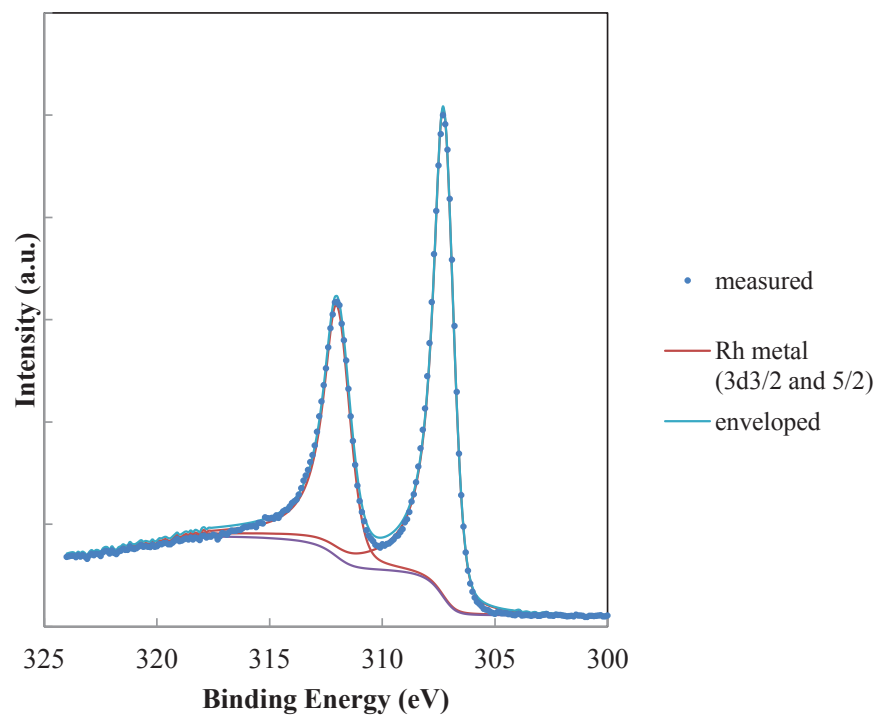| Rh species	Position (eV)	Fraction of species (%)
Rh metal	307.3	100

Fig.4-3. Analysis of deconvolved Rh 3d spectrum of sample (a) before exposure to NO.
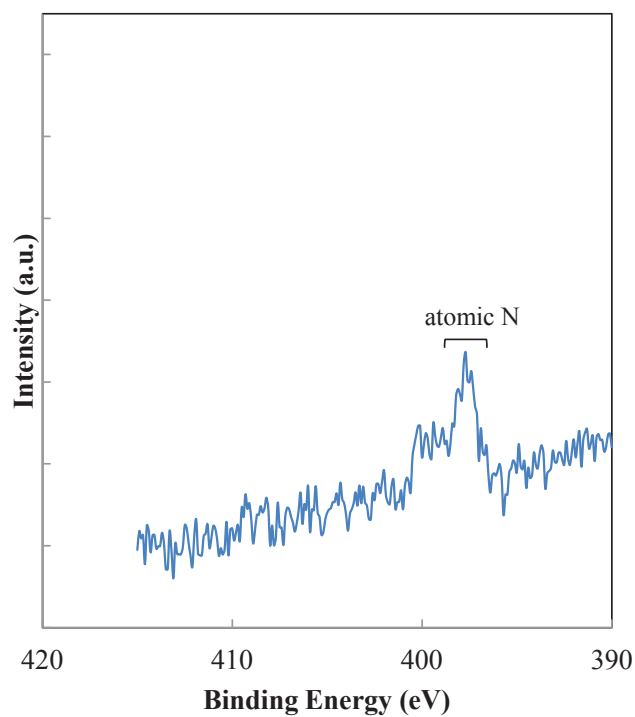

Fig.4-4. XPS N 1s spectrum of sample (a) before exposure to NO.

Next, NO gas was introduced to the deposited Rh nanoparticles without exposing the sample to ambient air. The electronic properties of sample (b) were measured, and Figures 4-5 and 4-6 show the Rh 3d and N 1s spectra of the sample. The peak top in the Rh $3d_{5/2}$ spectrum of sample (b) is located at 307.4 eV, and it is wider than the same peak in the Rh $3d_{5/2}$ spectrum of sample (a). When the Rh $3d_{5/2}$ spectrum for sample (b) was deconvolved, the resolved peaks of sample (a) fit those of sample (b), which means that, the Rh nanoparticles of sample (b) were also in the metallic state, including 7% of Rh_2O_3 (Table 2). These results indicate that part of the Rh surface changed to the Rh^{3+} state upon exposure to NO. In the N 1s spectrum of sample (b), three peaks appear at 397.5, 400,   and 403.5 eV, which correspond to atomic N, chemisorbed NO, and chemisorbed NO_2, respectively, according to the results of previous works [22, 23]. These results suggest that some NO molecules were directly chemisorbed on Rh metal, while others dissociated into atomic N and O, where the O atoms reacted with incoming NO molecules to form NO_2. Since NO_2 had the electron-withdrawing effect of oxygen at the surface, the surface of Rh nanoparticles could have had a different oxidation state [22, 23].

Table 4-2: Result of deconvolution analysis of Rh $3d_{5/2}$ spectrum of sample (b) after exposure to NO without ambient air.

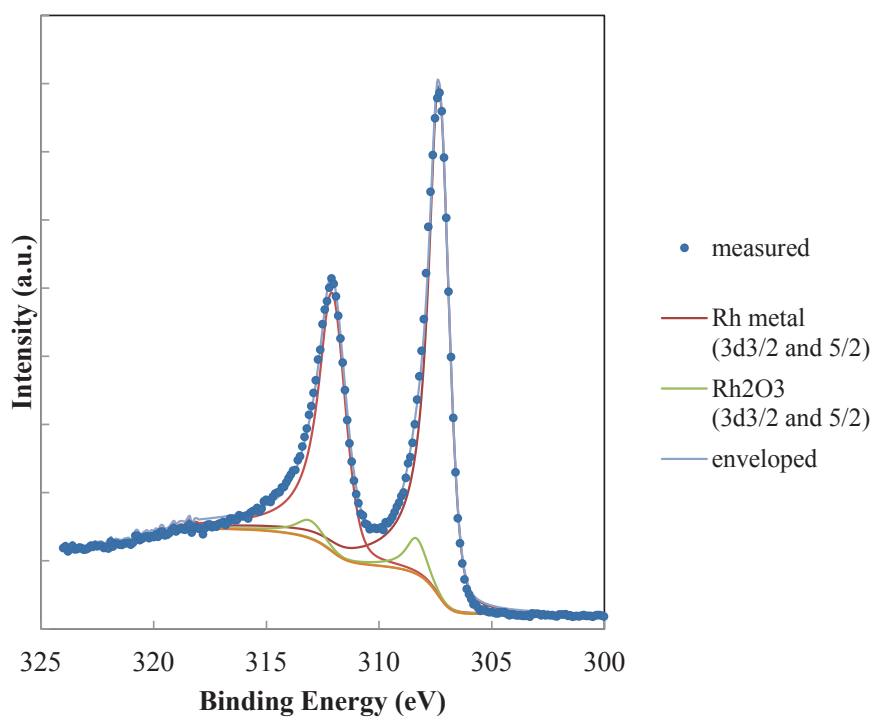| Rh species	Position (eV)	Fraction of species (%)
Rh metal	307.4	93
Rh_2O_3	308.4	7

Fig.4-5 Analysis of deconvolved Rh 3d spectrum of sample (b) after exposure to NO without ambient air.
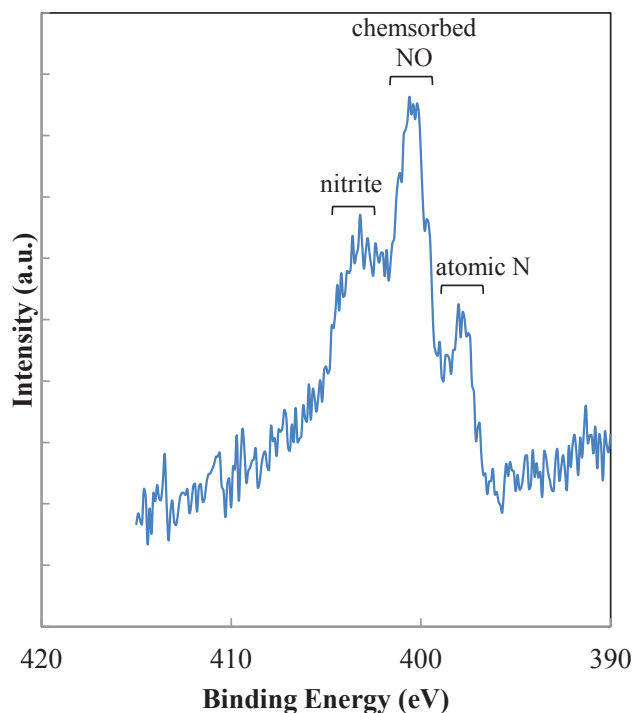
Fig.4-6. XPS N 1s spectrum of sample (b) after exposure to NO without ambient air.

Finally, the effect of ambient air on NO adsorption was examined. Figures 4-7 and 4-8 show the Rh 3d and N 1s spectra of the Rh nanoparticles, and the components corresponding to the for Rh $3d_{5/2}$ spectrum are summarized in Table 4-3. The peak in the Rh3 $d_{5/2}$ spectrum of sample (c) is located at 307.5 eV, with a peak at 308.6 eV. The deconvolution analysis indicates that the Rh nanoparticles in sample (c) were in the metallic state, including 13% of Rh_2O_3. In the N 1s spectrum, only a small peak corresponding to NO_2 appears at 403.0 eV possibly because the surface of the Rh nanoparticles was preferentially oxidized by O_2 from the ambient air, and a small amount of adsorbed NO reacted with the surface oxygen

to form NO_2.

Table 4-3: Result of deconvolution analysis of Rh $3d_{5/2}$ of spectrum (c) after exposure to NO in ambient air.

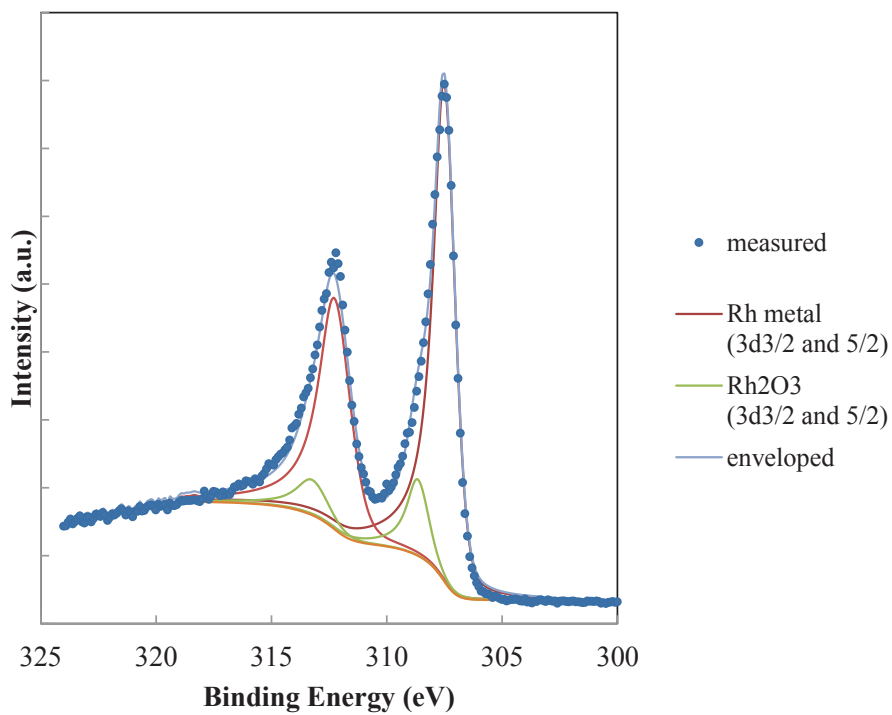| Rh species	Position (eV)	Fraction of species (%)
Rh metal	307.5	87
Rh_2O_3	308.6	13

Fig.4-7. Analysis of deconvolved Rh 3d spectrum of sample (c) after exposure to NO in ambient air.
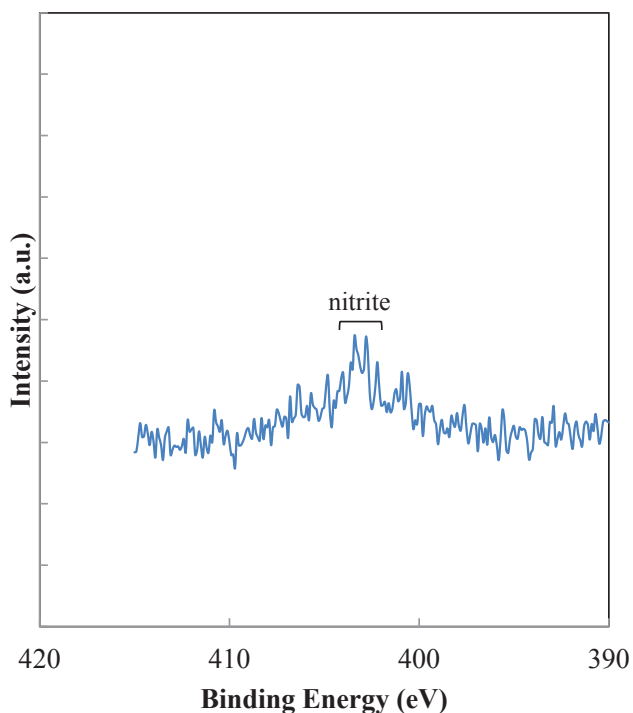
Fig.4-8.　XPS N 1s spectrum of sample (c) after exposure to NO in ambient air.

4.4 Conclusions

Adsorption of NO occurred when the surface of Rh nanoparticles remained in the metallic state. The *in-situ* SR-XPS analysis showed that chemisorbed NO, atomic N, and NO_2 were present on the Rh nanoparticles, and part of the Rh surface changed to the Rh^{3+} state. The presence of ambient O_2 led to a difference in the adsorption of NO on the Rh nanoparticles because O_2 preferentially oxidized the surface of the Rh nanopaticles and inhibited NO adsorption. *Ex-situ* XPS analysis showed that only a small amount of adsorbed NO reacted with the surface oxygen to form NO_2.

References

[1] H. Muraki, and G. Zhang, Catal. Today **63**, 337 (2000).

[2] H.S. Gandhi, G.W. Graham, and R.W. McCabe, J. Catal. **216**, 433 (2003).

[3] Q. Zheng, R. Farrauto, M.Deeba, and I. Valsamakis, Catalysts **5**, 1770 (2015).

[4] M. Vallden, X.Lai, and D.W. Goodman, Science **281,** 1647 (1998).

[5] M. Haruta, S. Tsubota, T. Kobayashi, H. Kageyama, M.J. Genet, and B. Delmon, J. Catal. **144**, 175 (1993).

[6] I. Lopez-Salido, D.C. Lim, and Y.D. Kim, Surf. Sci. **588**, 6 (2005).

[7] D.C. Lim, I. Lopez-Salido, and Y.D. Kim, Surf. Sci. **598**, 96 (2005).

[8] *F. Deushi, A. Ishikawa and H. Nakai, J. Phys. Chem. C, 121, 15272 (2017).*

[9] K. Ueda, K. Isegawa, K. Amemiya, K.Mase and H. Kondoh, ACS Catal., **8**, 11663 (2018).

[10] R. Toyoshima, M. Yoshida, Y. Monya, K. Suzuki, K. Amemiya, K. Mase, B. S. Mun and H. Kondoh, J. Phys. Chem. C **119**, 3033 (2015).

[11] H. Kawabata, Y. Koda, H. Sumida, M. Shigetsu, A. Takami, and K. Inumaru, Chem. Commun. **49**, 4015 (2013).

[12] H. Kawabata, Y. Koda, H. Sumida, M. Shigetsu, A. Takami, and K. Inumaru, Catal. Sci. Technol. **4**, 697 (2014).

[13] J. Gustafson, R. Westerstron, A. Resta, A. Mikkelsen, J.N. Andersen, O. Balmes, X. Torrelles, M. Schmid, P. Varga, B. Hammer, G. Kresse, C.J. Baddeley, and E. Lunggren, Catal. Today **145**, 227 (2009).

[14] S. Blomberg, R. Westerstron, N.M. Martin, E. Lundgren, J.N. Andersen, M.E. Messing, and J. Gustafson, Surf. Sci. **628**, 153 (2014).

[15] Y. Koda, H. Sumida, S. Ogawa, C. Tsukada, and H. Namatame, e-J. Surf. Sci. Nanotechnol. **15** 50 (2017).

[16] H. Niwa, S. Ogawa, K. Nakanishi, G. Kutluk, T. Ohta, and S. Yagi, J. Surf. Anal. 17, 278 (2011).

[17] M.P. Seah, I.S. Gilmore, and G. Beamson, Surf. Interface Anal. **26**, 642 (1998).

[18] J.F. Moulder, W.F. Stickle, P.E. Sobol, and K.D. Bomber, Handbook of X-ray Spectroscopy, J. Chastain (ed.), Perkin Elmer Corporation, Eden Prairie (1992).

[19] S. Kim, K. Qadir, S. Jin, A.S. Reddy, B. Seo, B.S. Mun, S.H. Joo, and J.Y. Park, Catal. Today **185**, 131 (2012).

[20] M.E. Grass, Y. Zhang, D.R. Butcher, J.Y. Park, Y. Li, H. Bluhm, K.M. Bratlie, T. Zhang, and G.A. Somorjai, Angew. Chem. Int. Ed. **47**, 8893 (2008).

[21] CasaXPS: Processing Software for XPS, AES, SIMS and More, http://www.casaxps.com/.

[22] R. Toyoshima, M. Yoshida, Y. Monya, K. Suzuki, K. Amemiya, K. Mase, B.S. Mun, and H. Kondoh. Surf. Sci. **615**, 33 (2013).

[23] A.-S. Mamede, G. Leclercq, E. Payen, P. Granger, L. Gengembre, and J. Grimplot. Surf. Interface Anal. **34**, 105 (2002).

Chapter 5

Characterization by synchrotron-radiation X-ray photoelectron spectroscopy of NO adsorption on Rh
- Effect of support material -

Chapter 5 Characterization by synchrotron-radiation X-ray photoelectron spectroscopy of NO adsorption on Rh

- Effect of support material –

5.1. Introduction

Catalysts play an important role in purifying exhaust gases to meet the stringent regulations for automobile emissions. From the point of view of fuel efficiency, automobile engines are required to operate under lean condition (high air-to-fuel ratio) which means that maintaining the performance in NO reduction becomes a serious issue. Rhodium is a precious metal that is essential to cutting NO emission by reducing nitrogen oxides to nitrogen and oxygen [1-3], and one way to make Rh more effective in NO reduction is minimizing the Rh particle size to maximize the number of reaction sites. As the metal particle size decreases below 10 nm, electronic and geometric properties that are different from those of the bulk material can be observed [4-7]. Another way to boost NO reduction is exploiting the Rh surface, whose electronic properties are suitable for NO adsorption. The first concern regarding effective use of Rh is understanding the intrinsic properties of Rh nanoparticles. *In-situ* X-ray photoelectron spectroscopy (XPS) is a suitable analytical

method for characterization of the electronic properties of Rh because it can exclude the effect of any adsorbed species. In our previous work, using synchrotron radiation (SR) XPS, we revealed that Rh nanoparticles that were not exposed to ambient air were in the metallic state [8]. After NO adsorption, part of the Rh surface changed to the Rh^{3+} state on the outermost surface and chemisorbed NO, atomic N, and NO_2 were present on the Rh nanoparticles [9]. Practical three-way catalysts are comprised of particles of precious metals such as platinum or palladium or rhodium, metal particles are supported on metal oxides, for example Al_2O_3, ZrO_2, and CeO_2 and so on [1-3]. Because not only they maintain their surface area and prevent the sintering of precious metals, but also control the reactivity by the interaction between metals and support materials. In the past studies, these interactions are due to the donating-accepting electrons between the metal nano-cluster and the oxide support materials, the active cite on these boundaries, the dispersive electronic state of the metal nano-cluster, the low coordination number of the surface atoms and so on [10, 11]. This interaction has been applied to commercial catalysts. Therefore, the effect of this interaction for the electronic property and NO adsorption behavior has to be clarified for development the next generation TWC.

To understand these mechanisms, a modeled catalyst using such as a wafer and a

size-controlled metal excluding the structural effect, *in-situ* analysis excluding the

effect of other adsorbates provide us very clear answers. Moreover, a combination

with theoretical calculations enables to understand the behaviors thermodynamically.

The purpose of this paper is to report effect of support materials on the electronic

properties of Rh nanoparticles and the behavior of NO molecules using *in-situ* XPS

with SR and theoretical calculations.

5.2. Experimental

5.2.1 Preparation of Rh nanoparticles

Rh nanoparticles were fabricated by the evaporation method [12] in a Rh

evaporation chamber. The evaporation chamber was connected to the load-lock

chamber of BL6N1 at the Aichi Synchrotron Radiation Center (Aichi SR) in Japan.

A Rh wire (4N) was evaporated to release Rh atoms and the Rh nanoparticles were

grown under 50 Torr of high-purity He gas (5N5). The nanoparticles were

transferred to the deposition chamber through a stainless steel pipe and deposited

on a grid, an n-type Si wafer with <100> orientation (SiO_2/Si wafer) and a CeO_2

thin film of about 10 nm thickness on an n-type Si wafer (CeO_2/Si wafer). The grid,

SiO_2/Si wafer and CeO_2/Si wafer were set in the depostion chamber as the

substrates of the transmission electron microscopy (TEM) and XPS samples, respectively.

5.2.2 Analysis of Rh nanoparticles under different conditions

TEM experiments were carried out using a transmission electron microscope (JEM-3000F, JEOL, Japan) at an accelerating voltage of 300 kV. To evaluate the size of the Rh nanoparticles, the dispersed Rh nanoparticles were deposited on the grid within a short period of time.

The chemical states of the Rh nanoparticles under different conditions were investigated by SR-XPS at BL6N1 in Aichi SR. The photon energy for XPS analysis was set at 2.0 keV. As the evaporation chamber for Rh nanoparticles was connected to the load-lock chamber, the Rh nanoparticles could be analyzed without exposure to ambient air. A NO (2% in He) gas cylinder was connected to the evaporation chamber and the NO gas was introduced after deposition of the Rh nanoparticles. X-ray photoelectron spectra were collected for two different samples of Rh nanoparticles: (a) before exposure to NO; (b) afteexposure to NO for 5 min.. The spectra were calibrated against the peak of Au $4f_{7/2}$ at 83.95 eV [13]. The binding energies of Rh $3d_{5/2}$ for metallic Rh, Rh_2O_3, and RhO_2 are 307.2, 308.2, and

309.5 eV, respectively [14-16], and the difference between Rh $3d_{5/2}$ and Rh $3d_{3/2}$ is 4.74 eV. The deconvolution analysis of the Rh $3d_{5/2}$ peaks was performed by CASA XPS [17], and each area of the Rh species with a different oxidation state was estimated as the fraction of that species in the deposited Rh nanoparticles. As a control experiment, a CeO_2/Si wafer without Rh nanoparticles was performed under same experiment to evaluate NO adsorption.

5.2.3 Theoretical calculations

All DFT calculations were performed by using DMol3 version 7.0 software. We carried out the spin-restricted calculation and employed the double numerical basis set with polarization functions and effective core pseudopotentials generated by fitting all-electron relativistic DFT results. As for the exchange-correlation functional, the generalized gradient approximation, RPBE, was used. For the CeO_2 surface, we used the 4 x 3 (111) surface consisting of six atomic layers and fixed bottom three layers of them during the structure optimization. Whereas for the SiO_2 surface, the 2 x 2 alpha-quartz (001) surface fully hydroxylated was used with fixing bottom six atomic layers of eleven layers in total except for hydrogen during the optimization. In both surface models, we used a vacuum layer of 15 Å and determined lattice

constants from previous unit-cell optimization of each oxide: a=b=c=5.526 for CeO_2, and a=b=5.069, c=5.572 for alpha-quartz SiO_2. In the Brillouin-zone integration, 2 x 2 x 1 and 2 x 3 x 1 Monkhorst-Pack k-point meshes were set for the CeO_2 system and SiO_2 one, respectively.

NO adsorbed on three-fold site of Rh4 cluster, and one layer of surface of the substrates and adsorbed NO were allowed to relax.

5.3. Results and Discussions

5.3.1 TEM study

The image and structural analysis of Rh nanoparticles on a SiO_2/Si wafer are in chapter 4. The TEM image of the Rh particles on a CeO_2/Si wafer in Figure 1 shows that particles with spherical shape were deposited. Using Figure 5-1, the size of the Rh particles was evaluated, and the size distribution of the Rh particles is shown in Figure 5-2. The diameter of the Rh particles varied from 2.1 to 5.5 nm, and the estimated average size was 3.6 ± 0.9 nm, where the standard deviation (S.D.) was used for the uncertainty.
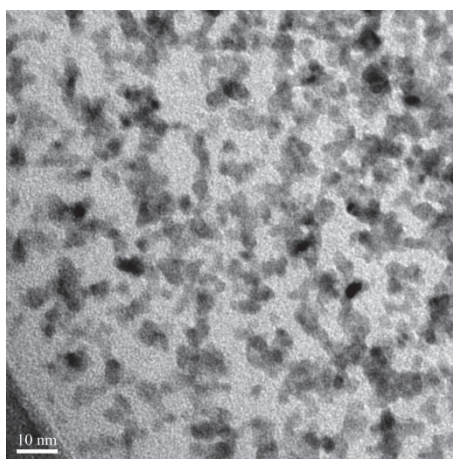
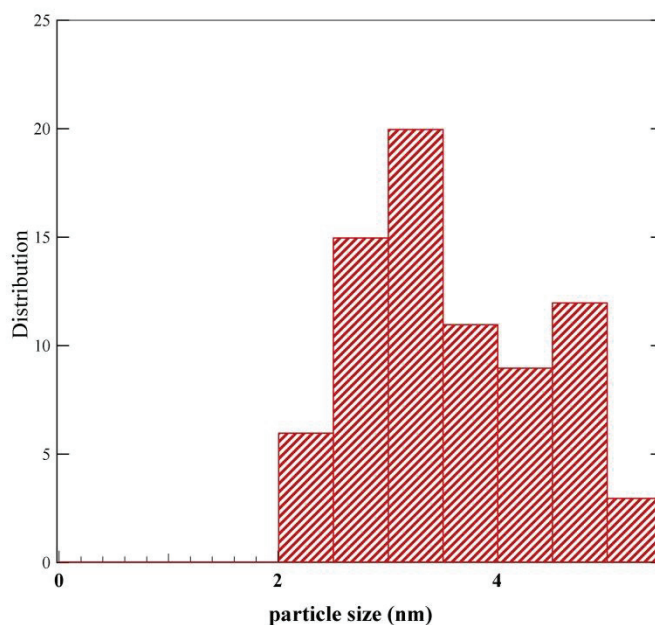Fig.5-1.   TEM image of Rh nanoparticles.

Fig.5-2.   Size distribution of Rh nanoparticles.

5.3.2 XPS analysis

The peaks of Rh 3d and Rh 3p, and the valence band can be found in the in- situ

XPS survey spectrum for sample (a) of Rh nanoparticles on a CeO_2/Si wafer, which

is not shown here. The peaks of O 1s and C 1s are absent, which means that the

nanoparticles that were not exposed to ambient air were in the metallic state and there was no contamination. This result is same as Rh nanoparticles on a SiO_2/Si wafer reported in Chapter 4. TEM images indicate that the Rh nanoparticles were deposited like a thin film on the substrate as same as Rh nanoparticles on SiO_2/Si. Here after, these are referred to as the "Rh nanoparticles".

Figures 5-3 and 5-4 show the Rh 3d and N 1s spectra of sample (a) of Rh nanoparticles on a CeO_2/Si wafer, and the components corresponding to the Rh $3d_{5/2}$ spectrum are summarized in Table 5-1. The peak in the Rh $3d_{5/2}$ spectrum of sample (a) is located at 307.3 eV. The deconvolution analysis indicates that the Rh nanoparticles in sample (a) were in the metallic state. This result is same as Rh nanoparticles on a SiO_2/Si wafer reported in Chapter 4. In the N 1s spectrum, no peaks could be found.

Table 5-1: Result of deconvolution analysis of Rh $3d_{5/2}$ spectrum of sample (a) before exposure to NO.

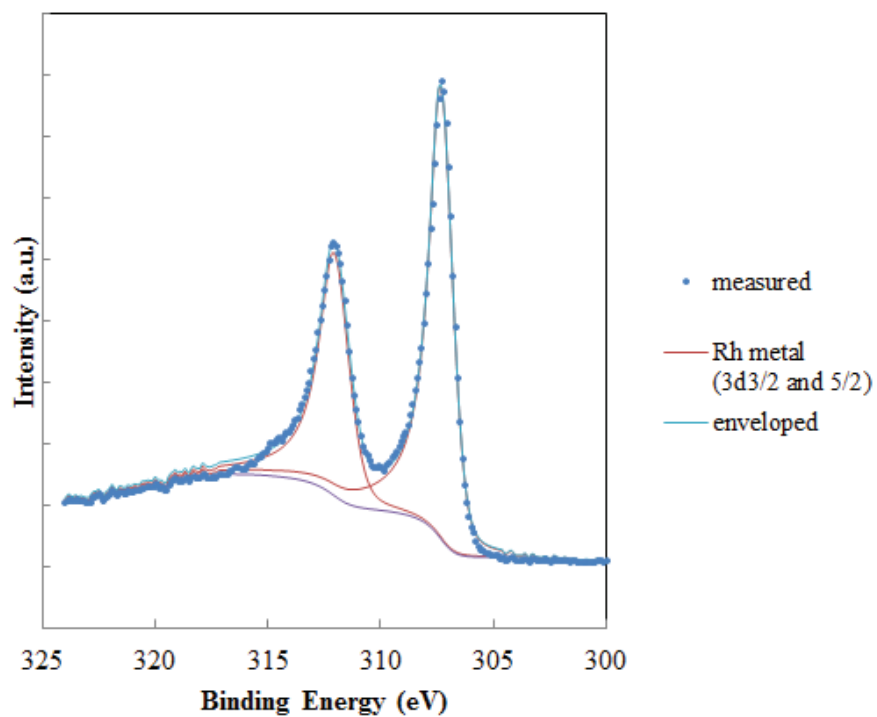| Rh species	Position (eV)	Fraction of species (%)
Rh metal	307.3	100

Fig.5-3. Analysis of deconvolved Rh 3d spectrum of sample (a) before exposure to NO.
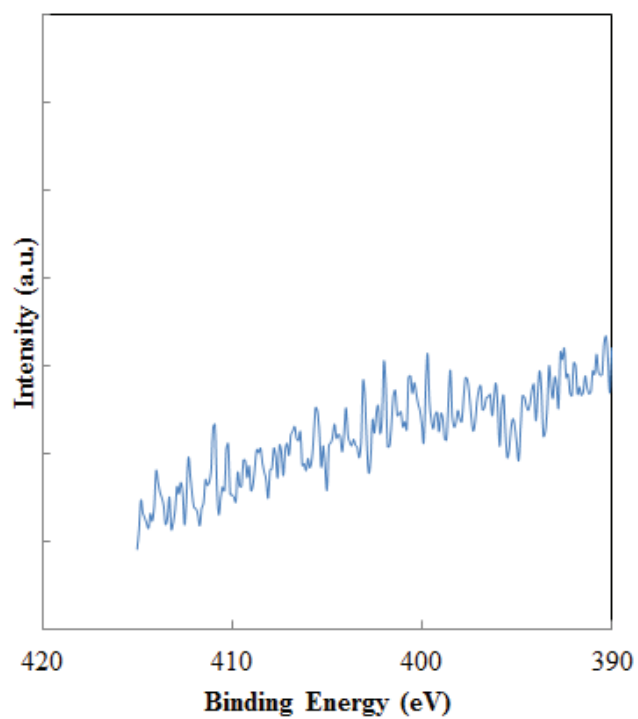

Fig.5-4. XPS N 1s spectrum of sample (a) before exposure to NO.

Next, NO gas was introduced to the deposited Rh nanoparticles without exposing the sample to ambient air. The electronic properties of sample (b) of Rh nanoparticles on a CeO_2/Si wafer were measured, and Figures 5-5 and 5-6 show the Rh 3d and N 1s spectra of the sample. The peak top in the Rh $3d_{5/2}$ spectrum of sample (b) is located at 307.3 eV, and it is wider than the same peak in the Rh $3d_{5/2}$ spectrum of sample (a). When the Rh $3d_{5/2}$ spectrum for sample (b) was deconvolved, the resolved peaks of sample (a) fit those of sample (b), which means that, the Rh nanoparticles of sample (b) were also in the metallic state, including 11% of Rh_2O_3 and 5% of RhO_2 (Table 5-2).

Table 5-2: Result of deconvolution analysis of Rh $3d_{5/2}$ spectrum of sample (b) after exposure to NO without ambient air.

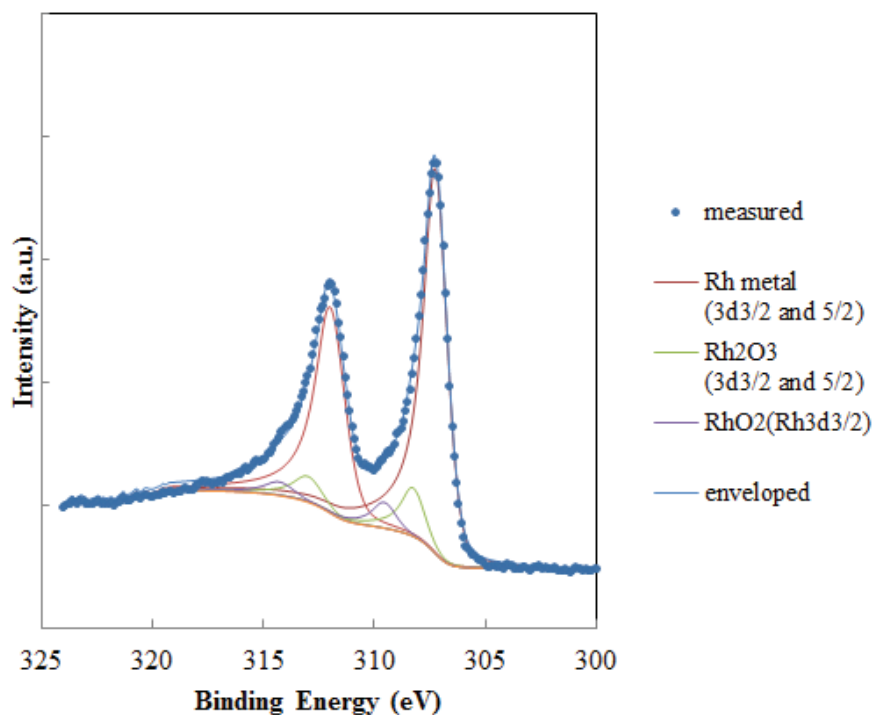| Rh species	Position (eV)	Fraction of species (%)
Rh metal	307.3	84
Rh_2O_3	308.3	11
RhO_2	309.6	5

Fig.5-5.　Analysis of deconvolved Rh 3d spectrum of sample (b) after exposure to NO without ambient air.
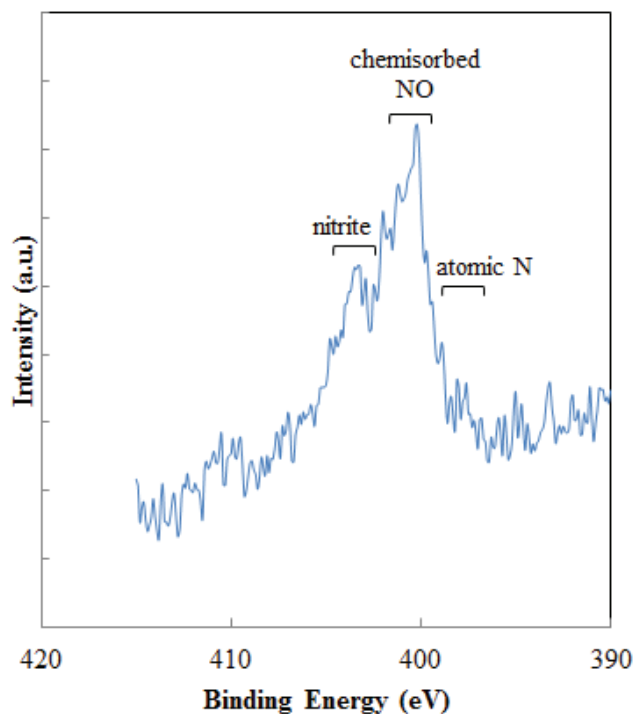

Fig.5-6.　XPS N 1s spectrum of sample (b) after exposure to NO without ambient air.

These results indicate that part of the Rh surface changed to the higher oxidation state of Rh upon exposure to NO. This result is same as Rh nanoparticles on a SiO$_2$/Si wafer reported in Chapter 4. But compared with Rh nanoparticles on a SiO$_2$/Si wafer and Rh nanoparticles on a CeO$_2$/Si wafer, Rh nanoparticles on a CeO$_2$/Si wafer has higher oxidation state than that of Rh nanoparticles on a SiO$_2$/Si wafer. In the N 1s spectrum of sample (b) of Rh nanoparticles on a CeO$_2$/Si wafer, two peaks appear at 400 and 403.6 eV, which correspond to chemisorbed NO and chemisorbed NO$_2$, respectively, according to the results of previous works [18, 19], but atomic N can't be found which appears on a SiO$_2$/Si wafer. These results suggest that some NO molecules were directly chemisorbed on Rh metal, while others dissociated into atomic N and O, where the O atoms reacted with incoming NO molecules to form NO$_2$. Since NO$_2$ had the electron-withdrawing effect of oxygen at the surface, the surface of Rh nanoparticles could have had a different oxidation state [18, 19]. And compared with these results, rate of the dissociation reaction from NO to N and O seemed to be higher on Rh nanoparticles on a CeO$_2$/Si wafer than those of a SiO$_2$/Si wafer. For a control experiment, we performed a same experiment with a CeO$_2$/Si wafer without Rh NP. Fig.5-7 shows the N 1s spectrum of sample (b) of a CeO$_2$/Si wafer. No peaks are found and this

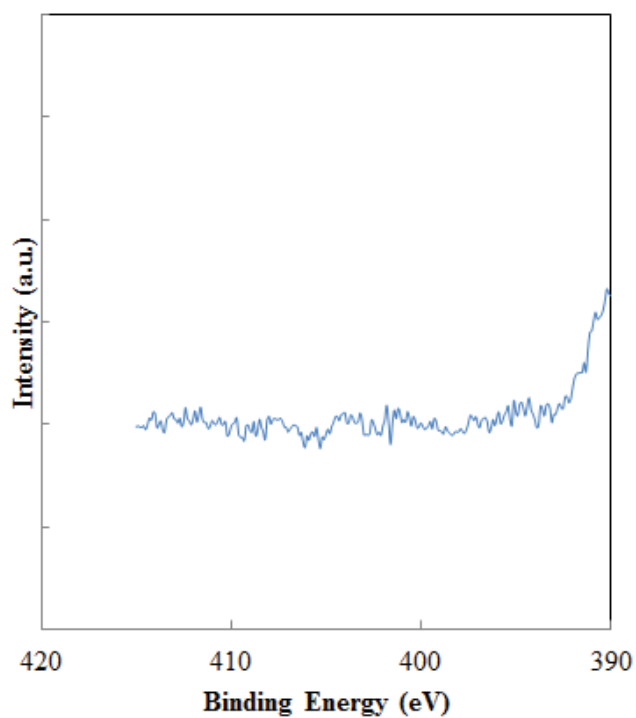indicates that peaks in Fig.5-6 were derived from absorbed NO and NO_2 on Rh NP.
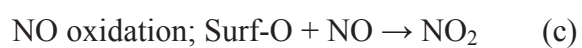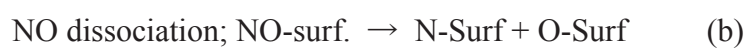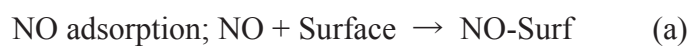

Fig.5-7. XPS N 1s spectrum of sample (b) of a CeO_2/Si wafer after exposure to NO without ambient air.

5.3.3 Theoretical calculations

For the result of XPS analyses, reactions are assumed as follows. Firstly, reactions caused by introduced NO are

NO adsorption; $NO + Surface \rightarrow NO\text{-}Surf$ (a)

NO dissociation; $NO\text{-}surf. \rightarrow N\text{-}Surf + O\text{-}Surf$ (b)

NO oxidation; $Surf\text{-}O + NO \rightarrow NO_2$ (c)

Secondly, reactions related to the lattice oxygens of support material are

Adsorbed NO + surface oxygen of support material → adsorbed NO_2;

Surf-NO + Surf(MO_x) → Surf-NO_2 + Surf(MO_{2-Vo})   (d)

Adsorbed N + surface oxygen of support material → adsorbed NO;

Surf-N + Surf(MO_x)   → Surf-NO + Surf(MO_{2-Vo})   (e)

Therefore, it is supposed that reactions (b) and (e) which are related to the formation of atomic N are influenced by the support materials.

Moreover, we will explain these behaviors thermodynamically by the theoretical calculations. We evaluated the reaction possibility by DFT calculations focusing on the reaction energy of reaction (b) and (e). In the previous study, it has been reported that even a small number of noble metal atoms can provide to sufficient effect to reproduce NO adsorption behavior. For this reason, four Rh atoms cluster on the support material has been adopted as a calculation model in this study. CeO_2 (111) or alpha-quartz SiO_2(001) were used for the support materials, and calculations were performed by Dmol^3 (Ver. 7.0 sp1). Each of The adsorption energy is calculated according equation (1) – (3) and the reaction energy is calculated according equation (4) and (5).

$$E(NOad) = E(Surf-NO) – [E(Surf) + E(NO)] \cdot \cdot \cdot \quad (1)$$

$$E(Nad) = E(Surf-N) + E(Surf) – 1/2\ E(N_2) \cdot \cdot \cdot (2)$$

$$E(Oad) = E(Surf\text{-}O) + E(Surf) - 1/2\ E(O_2) \cdot \cdot \cdot (3)$$

$$E(NO\ dissociation) = E(Nad) + (Oad) - E(Surf) - E(NOad) \cdot \cdot \cdot (4)$$

$$E(NO\ formation) = E(Surf(MO_{2\text{-}vo}\text{-}NO)) - E(Surf\text{-}N)\ \cdot \cdot \cdot (5)$$

The smaller the adsorption energy is, the stronger the gas molecule adsorbed. And the smaller the reaction energy is, the easier these reactions progress to the right side. In other words, in formula (4), NO is easy to dissociate. Part of reaction model is shown in Fig.5-8 and 5-9. In Table 5-3, the smallest reaction energy which means that NO dissociation is most likely to proceed among the calculation results of adsorption energies (formula (1) to (3)) was shown. Using these adsorption energy, the dissociation energy (b) [formura(4)] was calculated. As a result, under the condition that the reaction energy is smallest, which means most likely to disociate, the NO dissociation energies turned to be -1.52 eV for Rh4/SiO$_2$ and -1.47 eV for Rh4/CeO$_2$ (Table 5-6). This suggested that Rh4/SiO$_2$ has a process which NO dissociation progress a little easier than Rh4/CeO$_2$.
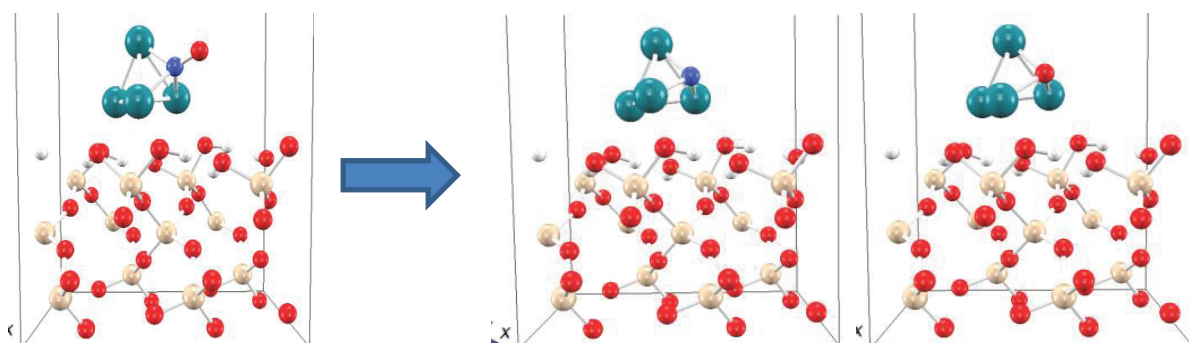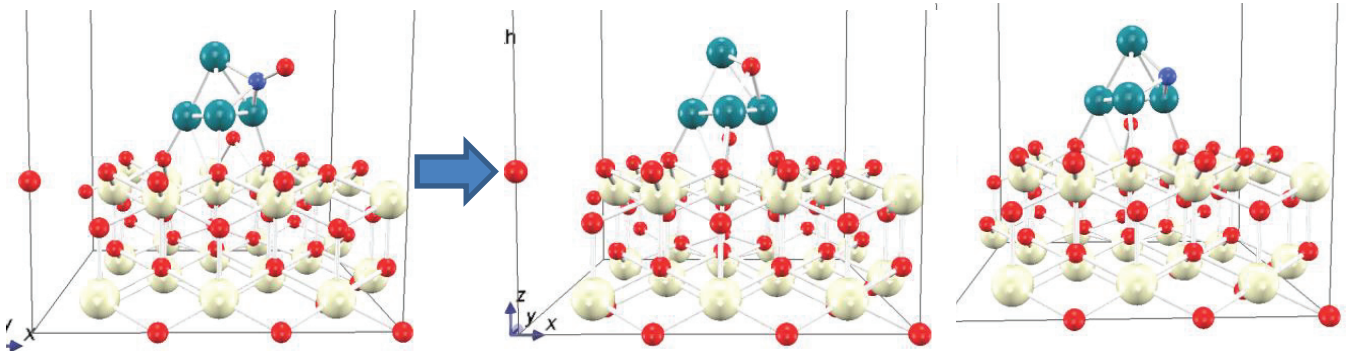

Fig.5-8　　NO dissociation model of Rh4/SiO$_2$

Fig.9　NO dissociation model of Rh4/CeO$_2$

Table 3　Adsorption energies and reaction energies calculated by DFT

sample	adsorbates	total E (Ha)	E(adsorption)/eV	E (NO dissociation)/eV
Rh/SiO2	–	−6463.49	–	−0.56
	NO	−6593.54	−2.52	–
	N	−6518.29	−0.38	–
	O	−6538.76	−1.89	–
Rh/CeO2	–	−5807.70	–	−0.38
	NO	−5937.75	−2.60	–
	N	−5862.50	−0.40	–
	O	−5882.96	−1.77	–

For the next step, the reaction energy of (e) was calculated. For formula (5), the first term on the right side indicates the energy of NO adsorption on Rh4 and the second term indicates the energy of N adsorption on Rh4, resulting that the energy for the oxidation of N with the surface oxygen of the support material. In this study, the structures which N and NO adsorb on the hollow site of Rh4 were adoped. And the oxygen of support material nearest N without bond to Rh4 was removed (Fig.5-10, 5-11).

Because all surface oxygen of SiO$_2$ were hydrated, in oxidation N, the hydrogen

was assumed to bind Si where oxygen exists. As a result of these calculations, the reaction energies turned to be 2.02 eV for Rh4/SiO$_2$ and 1.08 eV for Rh4/CeO$_2$ shown in Table 5-4. The reaction energy for Rh4/CeO$_2$ was about 1 eV lower than Rh4/SiO$_2$ and this means N on Rh4/CeO$_2$ was oxidised much easier than Rh4/SiO$_2$. In this study, as the adsorption site of N and NO and the position of oxygen vacancy were fixed, the calculated energies seem to have some vatiations. Because the adsorption energies calculated from farmula (1) − (3) have variaions of about 0.01eV order, we have supposed that the conclusion written above maintains.
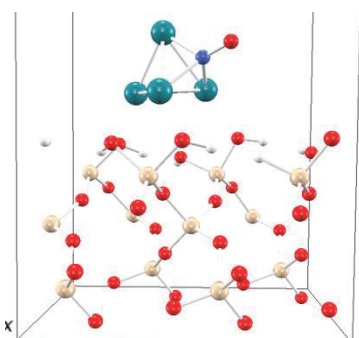

Fig.5-10 NO-Rh4/SiO$_2$ model whose an O of support surface was removed. (a dotted line circle indicates a place where an oxygen was removed and a new Si-H bond formed.)

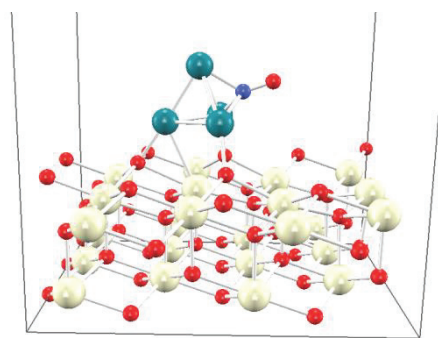Fig.5-11 NO-Rh4/CeO$_2$ model whose an O of support surface was removed. (a dotted line circle indicates a place where an oxygen was removed.)

Table 5-4   Reaction energies calculated by DFT

sample	adsorbates	total E (Ha)	E (NO formation)/eV
Rh/SiO$_{2-V_o}$	NO	−6518.22	2.02
Rh/SiO$_2$	N	−6518.29	−
Rh/CeO$_{2-V_o}$	NO	−5862.46	1.08
Rh/CeO$_2$	N	−5862.50	−

As a result of these calculations, it turned to be more difficult for $Rh4/CeO_2$ to have atomic N on Rh4 than $Rh4/SiO_2$. And this result has a same tendency of the result of the *in-situ* XPS.

In this study, the thermodynamic stability of each state was discussed by the reaction, which is the energy difference at the start and the end of the reaction. This is an advantageous method for evaluating the existence the existence probability of each state in the steady state. On the other hand, considering the activation energy which is the height of the energy barrier on the reaction coordinates connecting the start point and the end point, it seems that the phenomenon can be understood from the viewpoint of the reaction rate. Therefore, we will also evaluate activaion energy by DFT calculation in the future. At this time, the result of NO adsorption behavior obtained by *in-situ* XPS analysis could be explained by the adsorption stability (energy of each state) by DFT calculation. Furthermore, by carrying out detailed electronic state analysis such as the electron density of state, we will improve the accuracy of machnism clarificatkon and material development.

5.4. Conclusions

It has become clear that the behavior of NO molecules on Rh nanoparticles were different due to the support material by in-situ XPS analysis. Reaction energy regarding for atomic N was calculated using DFT method and these results correspond to the results of the analysis. The structural and electronic properties obtained by DFT calculations are useful for the machanism clarification and catalyst development.

References

[1] H. Muraki, and G. Zhang, Catal. Today **63**, 337 (2000).

[2] H.S. Gandhi, G.W. Graham, and R.W. McCabe, J. Catal. **216**, 433 (2003).

[3] Q. Zheng, R. Farrauto, M.Deeba, and I. Valsamakis, Catalysts **5**, 1770 (2015).

[4] M. Vallden, X.Lai, and D.W. Goodman, Science **281,** 1647 (1998).

[5] M. Haruta, S. Tsubota, T. Kobayashi, H. Kageyama, M.J. Genet, and B. Delmon, J. Catal. **144**, 175 (1993).

[6] I. Lopez-Salido, D.C. Lim, and Y.D. Kim, Surf. Sci. **588**, 6 (2005).

[7] D.C. Lim, I. Lopez-Salido, and Y.D. Kim, Surf. Sci. **598**, 96 (2005).

[8] Y. Koda, H. Sumida, S. Ogawa, C. Tsukada, and H. Namatame, e-J. Surf. Sci. Nanotechnol. **15** 50 (2017).

[9] Y. Koda, H. Sumida, S. Ogawa, C. Tsukada, and H. Namatame, e-J. Surf. Sci. Nanotechnol. **16** 36 (2018).

[10] 松本健俊, 表面科学 **27**, 6, 314 (2006).

[11] C. T. Cambell, Science **306**, 234 (2004), and references therein.

[12] H. Niwa, S. Ogawa, K. Nakanishi, G. Kutluk, T. Ohta, and S. Yagi, J. Surf. Anal. 17, 278 (2011).

[13] M.P. Seah, I.S. Gilmore, and G. Beamson, Surf. Interface Anal. **26**, 642 (1998).

[14] J.F. Moulder, W.F. Stickle, P.E. Sobol, and K.D. Bomber, Handbook of X-ray Spectroscopy, J. Chastain (ed.), Perkin Elmer Corporation, Eden Prairie (1992).

[15] S. Kim, K. Qadir, S. Jin, A.S. Reddy, B. Seo, B.S. Mun, S.H. Joo, and J.Y. Park, Catal. Today **185**, 131 (2012).

[16] M.E. Grass, Y. Zhang, D.R. Butcher, J.Y. Park, Y. Li, H. Bluhm, K.M. Bratlie, T. Zhang, and G.A. Somorjai, Angew. Chem. Int. Ed. **47**, 8893 (2008).

[17] CasaXPS: Processing Software for XPS, AES, SIMS and More, http://www.casaxps.com/.

[18] R. Toyoshima, M. Yoshida, Y. Monya, K. Suzuki, K. Amemiya, K. Mase, B.S. Mun, and H. Kondoh. Surf. Sci. **615**, 33 (2013).

[19] A.-S. Mamede, G. Leclercq, E. Payen, P. Granger, L. Gengembre, and J. Grimplot. Surf. Interface Anal. **34**, 105 (2002).

[20] F. Deuchi, A. Ishikawa and H. Nakai. J. Phys. Chem. C 2017, **121**, 15272

Chapter 6

Summary and General Conclusion

Chapter 6 Summary and General Conclusion

6.1 Summary of each Chapter

The subject of this thesis is to clarify the interaction between NO adsorption-desorption behavior which is the rate determining step of NO reduction and the electronic property of Rh used for active sites. Because the three-way catalyst for the next generation engine "HCCI" whose exhaust emission requires the higher performance at lower temperature under lean condition must be developed and this needs a drastic technical breakthrough, it is necessary to understand the true nature of the phenomenon as the first step for more effective catalyst development. Here are the summarized results obtained in each chapter.

6.1.1 Summary of Chapter 3

In Chapter 3, I characterize Rh nanoparticle itself. Rh nanoparticles have been fabricated by the evaporation method using the He gas in the Rh evaporation chamber, connected with the pre-evacuation chamber of BL6N1 at Aichi Synchrotron Radiation Center (Aichi SR) and the electronic and geometric properties of the Rh nanoparticles have been verified by *in-situ* XPS and *ex-situ*

XPS. Judging from the result of the in-situ XPS analysis, the Rh nanoparticles without atmosphere exposure is the Rh metallic state. On the other hand, by the *ex-situ* XPS analysis changing a photon energy, it became clear that the outermost surface changed into Rh_2O_3 and RhO_2.

6.1.2   Summary of Chapter 4

In Chapter 4, I characterized NO adsorption on Rh nanoparticles. Adsorption of NO occurred only when the surface of Rh nanoparticles remained in the metallic state. The *in-situ* SR-XPS analysis showed that chemisorbed NO, atomic N, and NO_2 were present on the Rh nanoparticles, and part of the Rh surface changed to the Rh^{3+} state. The presence of ambient O_2 led to a difference in the adsorption of NO on the Rh nanoparticles because O_2 preferentially oxidized the surface of the Rh nanopaticles and inhibited NO adsorption. *Ex-situ* XPS analysis showed that only a small amount of adsorbed NO reacted with the surface oxygen to form NO_2.

6.1.3   Summary of Chapter 5

In Chapter 5, I clarified the influence of the support material for NO adsorption on Rh nanoparticles. After Rh nanoparticles were deposited on a silicon wafer and

CeO_2 thin layer on a silicon wafer with a same method as in chapter 1 and were exposed to NO, the influence of the support material for NO adsorption on Rh nanoparticles was clarified. On the Rh nanoparticles on a SiO_2/Si wafer, chemisorbed NO, atomic N, and NO_2 were present. On the other hand, on the Rh nanoparticles on a CeO_2/Si wafer, chemisorbed NO and chemisorbed NO_2 were present. Futhermore, Rh nanoparticles on a CeO_2/Si wafer has higher oxidation state than that of Rh nanoparticles on a SiO_2/Si wafer after NO adsorption. These results show that CeO_2 tends to oxidize existence on its surface easier than SiO_2, in other words, CeO_2 has higher oxygen donating property than SiO_2. Moreover, reaction energy for NO dissciation was calculated using DFT method and these results correspond to the results of the analysis. This indicates that a combination with theoretical calculations enables to understand the behaviors thermodynamically.

6.2   General Conclusion

From the summary of each chapter, I will emphasize these clarifications written below.

Fabrication chamber is connected with the pre-evacuation chamber of Beam Line at Synchrotron Radiation XPS, and this enabled *in-situ* SR XPS analysis excluding the influence of any adsorbed components. Moreover, the load lock chamber of the Beam Line was used as a reaction chamber and the behavior of the adsorption gas could be evaluated at 760 Torr without ambient atmosphere. Analyses using these technique have revealed these results written below;

① *In-situ* and *ex-situ* SR XPS reveals that the surface of the Rh nanoparticles can easily change from the metallic state into Rh_2O_3 *and* RhO_2 itself.

② Adsorption of NO occurred only when the surface of Rh nanoparticles remained in the metallic state. The presence of ambient O_2 preferentially oxidized the surface into Rh_2O_3 and RhO_2 of the Rh nanopaticles and inhibited NO adsorption.

③ The support material influences NO adsorption-desorption behavior of Rh nanoparticles. Reaction energy regarding for atomic N was calculated using DFT method and these results correspond to the results of the analysis. The structural and electronic properties obtained by DFT calculations are useful for the machanism clarification and catalyst development. Changing photon energy of SR

soft XPS enables to evaluate not only the adsorption gas but also from Rh surface near the adsorption point to the deeper area near the support material that is based on the practical catalyst. Analyses using these techniques have revealed that in oxidation condition the surface of Rh NP changes into Rh_2O_3 and RhO_2 and the deeper area near the support material changes into higher oxidation state. This result indicates Rh-support material interaction can be evaluated by SR XPS.

These findings about the intrinsic properties of Rh nanoparticles become valuable for development of the next-generation three-way catalyst. Moreover, our strategy for clarification of the mechanism with combination analyzes and theoretical calculations can represent a first possible step toward material model base research. From now on, I will contribute to improve characterization accuracy and modeling calculation to clarify the electronic property accelerating MBR for material development.

ACKNOWLEDGEMENT